J. Fluid Mech. (2010), *vol.* 663, *pp.* 293–330.
doi:10.1017/S0022112010003526

Generation and breakup of Worthington jets after cavity collapse. Part 1. Jet formation

STEPHAN GEKLE[1,2] AND J. M. GORDILLO[3]†

[1]Department of Applied Physics and J. M. Burgers Centre for Fluid Dynamics, University of Twente, PO Box 217, 7500 AE Enschede, The Netherlands

[2]Physik Department, Technische Universität München, 85748 Garching, Germany

[3]Área de Mecánica de Fluidos, Departamento de Ingeniería Aeroespacial y Mecánica de Fluidos, Universidad de Sevilla, Avenida de los Descubrimientos s/n 41092, Sevilla, Spain

(Received 12 March 2010; revised 28 June 2010; accepted 29 June 2010; first published online 15 October 2010)

At the beginning of the last century Worthington and Cole discovered that the high-speed jets ejected after the impact of an axisymmetric solid on a liquid surface are intimately related to the formation and collapse of an air cavity created in the wake of the impactor. In this paper, we combine detailed boundary-integral simulations with analytical modelling to describe the formation of such Worthington jets after the impact of a circular disk on water. We extend our earlier model in Gekle *et al.* (*Phys. Rev. Lett.*, vol. 102, 2009*a*, 034502), valid for describing only the jet base dynamics, to describe the whole jet. We find that the flow structure inside the jet may be divided into three different regions: the axial *acceleration region*, where the radial momentum of the incoming liquid is converted to axial momentum; the *ballistic region*, where fluid particles experience no further acceleration and move constantly with the velocity obtained at the end of the acceleration region; and the jet *tip region*, where the jet eventually breaks into droplets. From our modelling of the ballistic region we conclude that, contrary to the case of other physical situations where high-speed jets are also ejected, the types of Worthington jets studied here cannot be described using the theory of hyperbolic jets of Longuet-Higgins (*J. Fluid Mech.*, vol. 127, 1983, p. 103). Most importantly, we find that the velocity and the shape of the ejected jets can be well predicted at any instant in time with the only knowledge of quantities obtained before pinch-off occurs. This fact allows us to provide closed expressions for the jet velocity and the sizes of the ejected droplets as a function of the velocity and the size of the impactor. We show that our results are also applicable to Worthington jets emerging after the collapse of a bubble growing from an underwater nozzle, although this system creates thicker jets than the disk impact.

Key words: aerosols/atomization, breakup/coalescence, bubble collapse, drops, jet formation, solid-liquid impact

1. Introduction

The impact of a solid object against a liquid interface is frequently accompanied by the ejection of a high-speed jet emerging out of the liquid bulk into the air. Figure 1,

† Email address for correspondence: jgordill@us.es

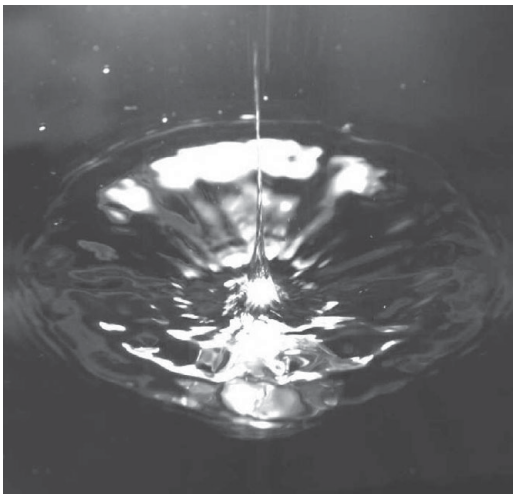

FIGURE 1. Image from above of the high-speed upward jet ejected into the atmosphere when a circular disk impacts perpendicularly against an air–liquid interface. In this paper, we will treat axisymmetric jets, an assumption which is well justified by the near-axisymmetric shape of the jet despite some non-axisymmetric disturbances visible at the jet tip and around the base.

which shows the effect of a horizontal disk that impacts on a pool of water, illustrates a liquid jet which flows $\sim$20 times faster than the disk impact speed. The qualitative description of this common and striking phenomenon was first elucidated at the beginning of the twentieth century by Worthington & Cole (1897, 1900). Through the careful analysis of the photographs taken after a solid sphere was dropped into water, Worthington & Cole (1897, 1900) realized that these types of liquid threads emerge as a consequence of the collapse of the air-filled cavity which is created at the wake of the impacting solid. They also made the remarkable observation that the generation of such cavities was very much influenced by the surface properties of the spherical solid. Decades after their original observations, May (1951) and Duez *et al.* (2007) quantified the conditions that determine the existence of the air cavity in terms of the surface properties of the solid and the material properties of the liquid.

High-speed jets emerging out of a liquid interface are also frequently observed in many other situations. For instance, it is very usual to perceive that the liquid 'jumps' out of the surface of sparkling drinks, a fact which is known to happen as a consequence of bubbles bursting at the liquid interface (Boulton-Stone & Blake 1993; Duchemin *et al.* 2002; Liger-Belair, Polidori & Jeandet 2008; Thoroddsen *et al.* 2009). Less familiar situations such as those related to the focusing of capillary (MacIntyre 1968; Thoroddsen, Etoh & Takehara 2007*b*) or Faraday waves (Hogrefe *et al.* 1998; Zeff *et al.* 2000) also give rise to the same type of phenomenon. In all the cases enumerated above, surface tension plays an essential role in the jet formation process. However, there are also many types of jets created by purely inertial mechanisms, such as those generated by pressure waves (Blake *et al.* 1993; Ohl & Ikink 2003; Antkowiak *et al.* 2007; Tjan & Phillips 2007) or those ejected after cavity collapse, which is the case analysed here.

All these jets share a common feature: they are ejected as a consequence of a very large axial pressure gradient created at the jet base, which is the region where the jet meets the bulk of the liquid. This indicates that there exist, at least, two

main characteristics that differentiate the many types of high-speed jets appearing in nature: the way the large overpressures are created and the length scale at which pressure variations take place. For instance, in Antkowiak *et al.* (2007), a large axial impulse pressure gradient originates near the bottom of a curved interface after the sudden deceleration of a liquid mass. Moreover, pressure variations occur at a length scale which is fixed by the radius of curvature of the interface. The associated pressure gradients are proportional to the product of the impact velocity times the aspect ratio of the cavity, which is of order unity and, consequently, Antkowiak *et al.* (2007) find that the initial jet velocity is of the order of 1–4 times the impact velocity.

In the case of Worthington jets created after cavity collapse, the overpressure originates from the radial deceleration experienced by the liquid at the jet base, and this overpressure deflects the flow in the axial direction. Note that whereas in the case studied by Antkowiak *et al.* (2007) the axial pressure gradient is created at one instant – just after the impact – in our case the axial pressure gradient is created continuously while the cavity is collapsing. In addition, in the case of Worthington jets after cavity collapse, energy is focused at length scales much smaller than those imposed by the geometry of the impactor and, consequently, the ratio of jet velocity to impact velocity can be as high as 20. We will show later that, in the case under study here, the jet velocity is proportional to the impact velocity divided by a non-trivial power of the radius of the jet at its base. As will become clear from the forthcoming discussion, this length scale varies in time and is not imposed by the geometry, but by the dynamical process taking place near the jet base.

Also, the impact of a drop on a liquid interface or solid surface (Oguz & Prosperetti 1990; Shin & McMahon 1990; Rein 1993; Morton, Rudman & Liow 2000; Howison *et al.* 2005; Bartolo, Josserand & Bonn 2006; Yarin 2006; Deng, Anilkumar & Wang 2007) is commonly accompanied by the ejection of columnar jets or liquid sheets whose velocities can be substantially larger than that of the impacting drop. These processes share some similarities with the type of Worthington jets considered here since, in our case, the high-speed jet is caused by the radial 'impact' of the flow along the axis of symmetry. In addition, Worthington jets ejected after cavity collapse are very similar in nature to the very violent jets of fluidized metal which are ejected after the explosion of lined cavities (e.g. Birkhoff *et al.* 1948), to those jets formed when an axisymmetric bubble collapses inside a stagnant liquid pool (Manasseh, Yoshida & Rudman 1998; Bolanos-Jiménez *et al.* 2008) or even to the granular jets observed when an object impacts a fluidized granular material (Thoroddsen & Shen 2001; Lohse *et al.* 2004). Because of the axisymmetric geometry of Worthington jets and their intrinsic unsteady nature, classical two-dimensional conformal mapping methods (see e.g. Gurevich 1966) cannot be applied in this case.

Most of the results presented here refer to the perpendicular impact of a circular disk with radius R_D and constant velocity V_D against a liquid surface. The fact that the solid is a disk instead of a sphere leads to the formation of an air cavity which is attached at the disk periphery, independent of the surface properties. Thus, this choice for the solid geometry avoids the additional difficulty of determining the position of the void attachment line on the solid surface. The differences pointed out above set our system somewhat apart from other impact studies (Glasheen & McMahon 1996; Duclaux *et al.* 2007; Duez *et al.* 2007; Grumstrup, Keller & Belmonte 2007; Aristoff & Bush 2009; Do-Quang & Amberg 2009). The experimental realization of the setup to which the numerical simulations presented are referred is described by Bergmann *et al.* (2006, 2009) and Gekle *et al.* (2008, 2009*a*), who show that boundary-integral simulations are in agreement with experiments.

In addition to disk impact, we also report potential flow numerical simulations to study the Worthington jets ejected after bubble pinch-off from an underwater nozzle sticking into a quiescent pool of water (Longuet-Higgins, Kerman & Lunde 1991; Oguz & Prosperetti 1993; Manasseh *et al.* 1998; Burton, Waldrep & Taborek 2005; Keim *et al.* 2006; Gordillo, Sevilla & Martínez-Bazán 2007; Thoroddsen, Etoh & Takehara 2007*a*, 2008; Bolanos-Jiménez *et al.* 2008; Burton & Taborek 2008; Gordillo 2008; Schmidt *et al.* 2009). As in the case of Worthington jets ejected after solid-body impact, similar boundary-integral simulations have been shown to be in agreement with experiments (see Oguz & Prosperetti 1993; Gordillo *et al.* 2007; Bolanos-Jiménez *et al.* 2008).

This paper is organized as follows. In § 2 we compare experimental results with boundary-integral simulations and review the main results of our earlier paper (Gekle *et al.* 2009*a*). In § 3 we analyse the structure of the liquid velocity field within the jet and divide the jet into the acceleration, ballistic and tip regions. In § 4, contrary to what could be expected from the analogy with other related physical situations, we show that Worthington jets ejected after cavity collapse cannot be described using the theory of hyperbolic jets developed by Longuet-Higgins (1983) and Longuet-Higgins & Oguz (1995). In § 5 we provide closed-form expressions for the velocity and the diameters of the drops ejected from the tip of the jet as a function of the impact velocity, the size of the impactor and the cavity pinch-off radius. Section 6 is dedicated to extending the results of the previous sections to the case of jets created after bubble pinch-off from a submerged nozzle. Finally, conclusions are drawn in § 7.

2. Experimental validation of the axisymmetric boundary-integral method and revision of previous results

The process of impact of a disk on a free surface (see also Bergmann *et al.* 2006, 2009; Gekle *et al.* 2009*a*) is illustrated in figure 2: after impact, a large cavity is created beneath the surface. Shortly after, this cavity collapses about halfway due to the hydrostatic pressure from the liquid bulk and, from the closure location, two high-speed jets are ejected upwards and downwards. Here positions, velocities and time are made dimensionless using as characteristic quantities the disk radius R_D, the impact velocity V_D and $T_D = R_D/V_D$, respectively. The main dimensionless parameters that control the sequence of events shown in figure 2 are the Froude number, $Fr = V_D^2/(R_D\, g)$, and the Weber number, $We = \rho V_D^2 R_D/\sigma$, where ρ and σ indicate the liquid density and the interfacial tension coefficient, respectively. The Reynolds number based on the impact velocity and the disk radius is $Re = V_D\, R_D/\nu \gg 1$, with ν as the kinematic viscosity of the liquid, whereas the local Reynolds number based on the jet size and the jet speed is of the order of 10^4, as shown in figure 3. Therefore, since viscous effects are negligible both at the disk and the jet scales, we will not include the Reynolds number as a control parameter. Moreover, since $We = \rho V_D^2 R_D/\sigma \gg 1$, surface tension effects are negligible in the first approach (see Gekle *et al.* 2009*a* for details) and, thus, the relevant control parameter for our experiments is only the Froude number.

From now on, variables in capital letters will be used to denote dimensional quantities and their lower-case analogues will indicate the corresponding dimensionless variable. Moreover, for both analytical and numerical purposes it will be assumed that axisymmetry is preserved and, thus, a polar coordinate system (r, z) will be used. The origins of both the axial polar coordinate z and time t are set at the cavity pinch-off height and at the pinch-off instant, respectively.

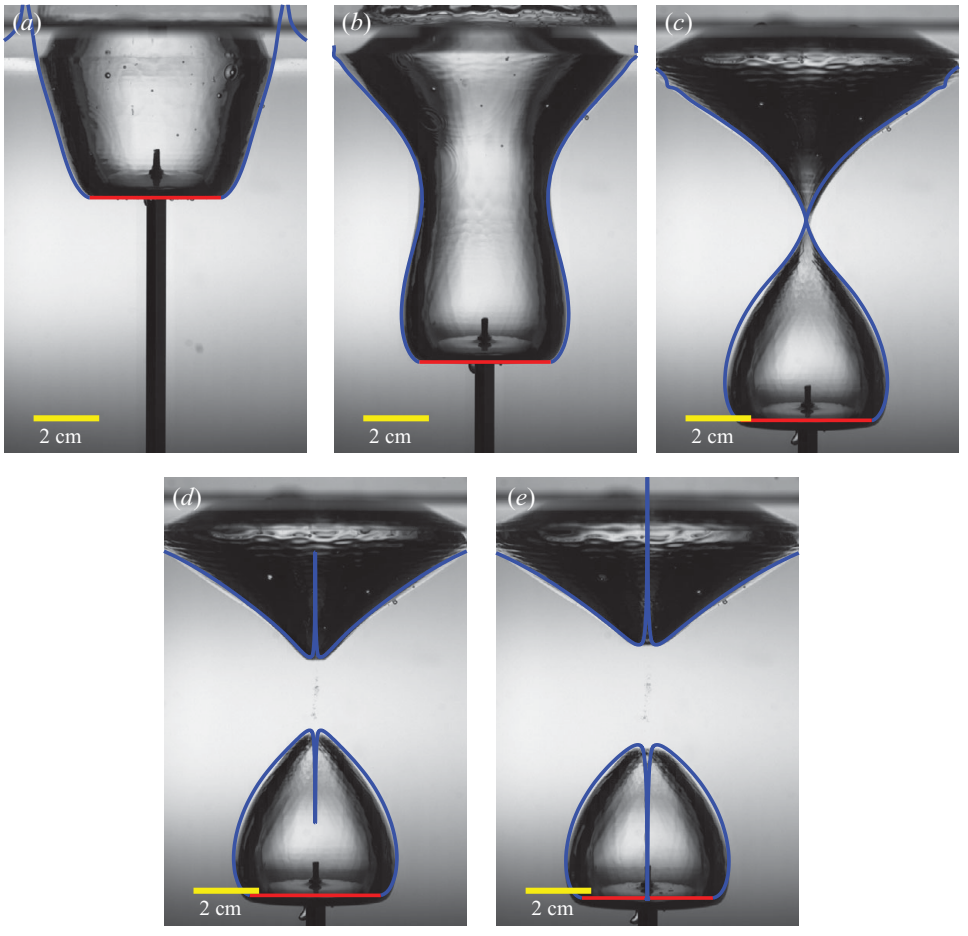

FIGURE 2. (Colour online) Experimental results obtained when a circular disk impacts perpendicularly and at constant velocity on a flat liquid interface, with $Fr = 5.1$, which is constant in time. Upon impact (*a–c*) a cavity attached to the disk periphery is created in the liquid which collapses under the influence of hydrostatic pressure. As a consequence of the cavity collapse, two jets with velocities much larger than that of the impacting solid, are ejected upwards and downwards (*d*, *e*). Note that the boundary-integral numerical simulation (in blue/grey) reproduces not only the collapse of the cavity but also the jet ejection process. The details of the comparison between experiments and numerical results in the complex region where the jet is ejected are more clearly shown in figure 4.

2.1. *Verification of the potential flow approach*

The results presented in this paper are largely based on axisymmetric boundary-integral simulations, which are known to provide good results whenever vorticity is confined to thin boundary layers. The only difference between the numerical code used here to simulate the ejection of the jet and that employed by Bergmann *et al.* (2009) is that, in the present axisymmetric simulations, it is necessary to impose an *ad hoc* cutoff radius, r_{min}, which we fix here to $r_{min} = 0.01$. The cutoff length r_{min} represents the value of the minimum radius of the cavity at which we impose the topological transition between a continuous, single cavity, into two separate cavities (see Appendix B for numerical details). This means that r_{min} acts as a filter that circumvents the difficulty of resolving the tiny time and spatial scales involved near

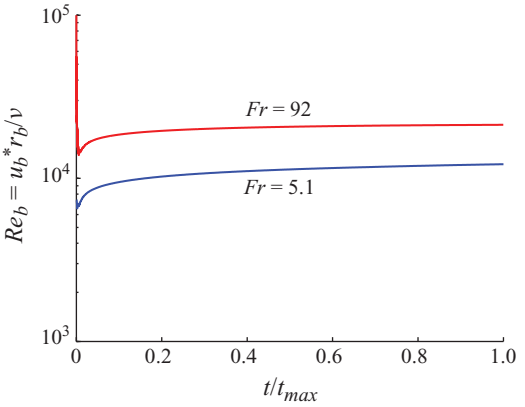

FIGURE 3. (Colour online) The high values of the local Reynolds number defined at the jet base justify our assumption of inviscid flow. Here $r_b(t)$ is the jet base radius and $u_b(t)$ is the time-dependent axial velocity calculated at this point. The point defined as the jet base, where the interface reaches a local minimum, is shown by a diamond in figure 4 and its definition is also sketched in figure 14, where the radial ($r_b(t)$) and axial ($z_b(t)$) coordinates of this important point are also indicated. To facilitate the comparison between the different Froude cases, times have been normalized by t_{max}, the time when the downward jet hits the disk and the simulation stops.

the topological transition. This simplification is necessary since, among other things, our code assumes axisymmetry and does not take into account gas inertia, although at these small scales both air (Gordillo *et al.* 2005; Gekle *et al.* 2010) and azimuthal asymmetries (Keim *et al.* 2006; Schmidt *et al.* 2009) greatly influence the pinch-off process. The simplification of fixing r_{min}, however, only affects a tiny portion of the jet – the jet tip – as shown in Appendix A.

To check the validity of the potential flow approach, we have compared several experiments with the numerical results. One of these comparisons is shown in figure 2(*a–c*), where it is shown that the agreement between simulation and experiment is excellent. Our numerical simulations are also in good agreement with experiments after pinch-off, as shown in figure 4. Note also that in figure 4 we define a crucial quantity characterizing the jet: the local free surface minimum which will be called, in what follows, the 'jet base' (see also figure 14, where the location of the jet base is sketched). The radial and vertical positions of this point shall be denoted by $r_b(t)$ and $z_b(t)$, respectively.

Other evidence that reinforces the validity of the axisymmetric potential flow approach to describe not only the cavity collapse but also the jet ejection process is provided in figure 5. This figure compares the numerical solution with experimental values of r_b and z_b. Observe that, for the two different values of the Froude number considered – and especially for the case $Fr = 10.6$ – the numerical solution (magenta line) is in fair agreement with experiments.

Let us emphasize here that, as shown in Appendix A, the good agreement between experiments and numerical results does not depend on the specific value of r_{min}: the same good agreement would be found whenever $r_b > r_{min}$ for any chosen value of r_{min}.

2.2. *Influence of the Froude number on the cavity shape*

Once we have demonstrated that we can resort to boundary integral simulations to reliably predict the time evolution of jets ejected after the collapse of axisymmetric

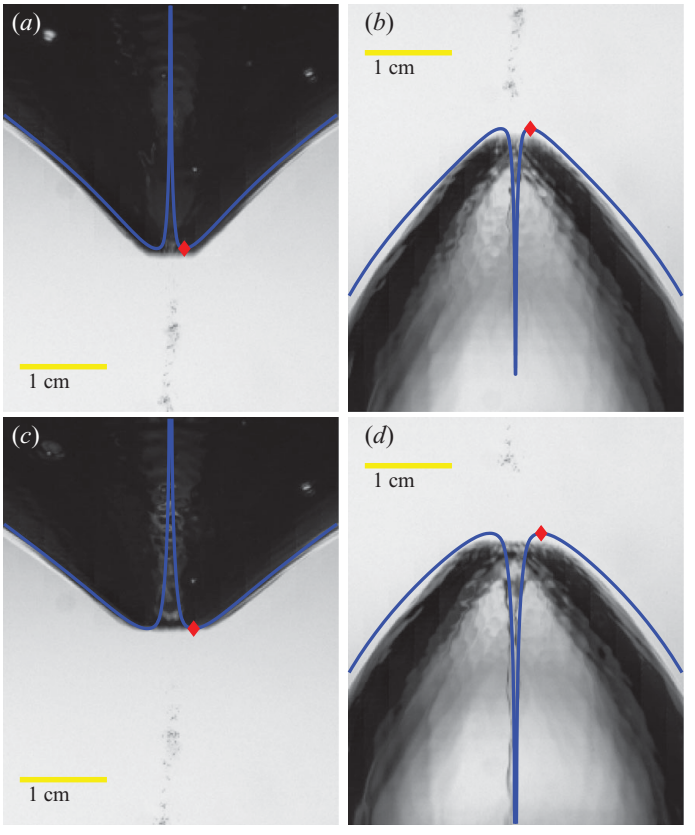

FIGURE 4. (Colour online) Magnification of the jet region corresponding to the two pictures located at the bottom row of figure 2. (*a–d*) The details of the emergence process of both the upward and downward jets observed in figure 2(*d*, *e*) are shown. Observe that the boundary-integral simulation closely follows the time evolution of the jet base region observed experimentally. The jet base is shown by a diamond.

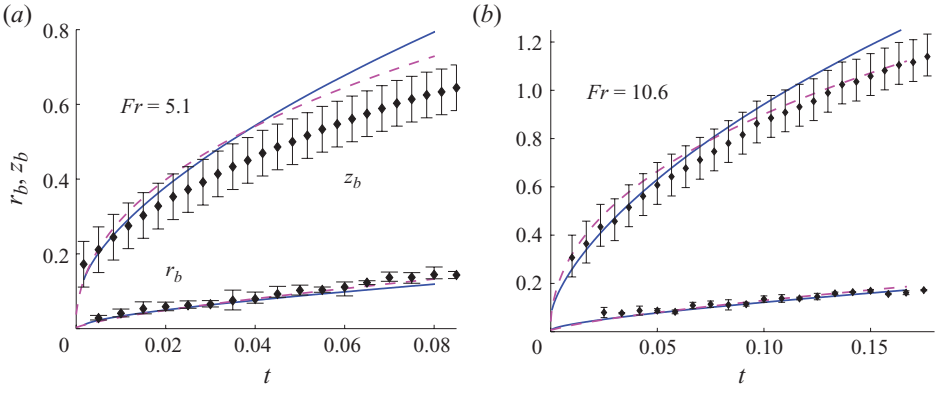

FIGURE 5. (Colour online) The dynamics of the jet base from the experiments (black diamonds) agrees rather well with the numerical simulations (dashed magenta line) and the analytical model (solid blue line) described in § 2.3 and Gekle *et al.* (2009*a*). The constants for the model are $C = 4.55$ and $C_{sink} = 0.63$ in (*a*) and $C = 5.5$, $C_{sink} = 0.63$ in (*b*).

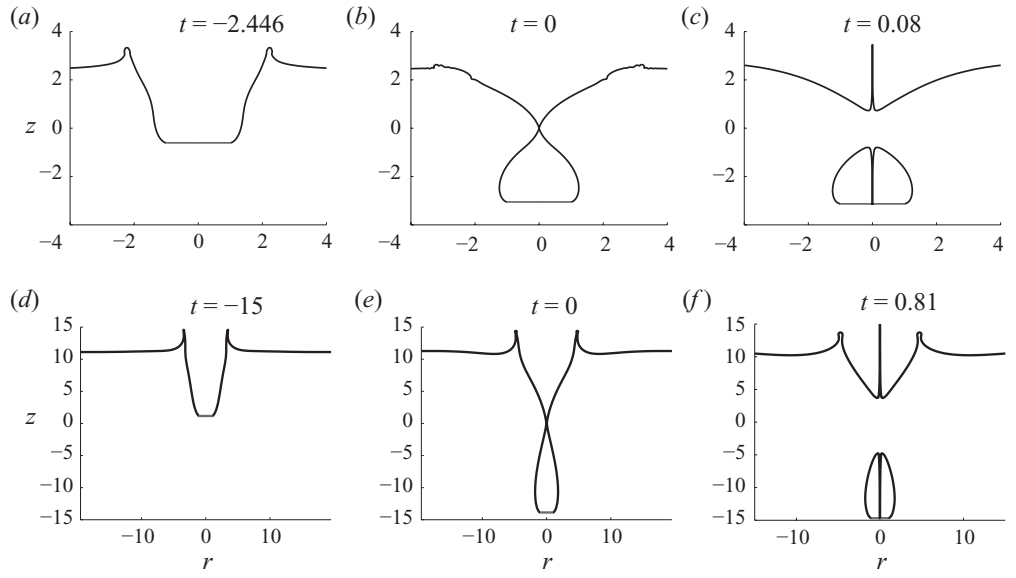

FIGURE 6. (*a–c*) Numerical results corresponding to the experimental images in figure 2 for a circular disk (horizontal blue line) impacting perpendicularly and at constant velocity on a flat liquid interface: cavity formation (*a*, *d*), collapse (*b*, *e*), and jet formation (*c*, *f*). The consequence of increasing the impact Froude number from $Fr = 5.1$ (*a–c*) to $Fr = 92$ (*d–f*) is that the cavity becomes more slender.

cavities, we can easily investigate the influence of the impact speed (quantified by the Froude number) on the different stages of the jet formation process. This is illustrated in figure 6, where it can be observed that larger Froude numbers create more slender cavities and also increase the non-dimensional depth at which the cavity closes. Furthermore, it can be appreciated that the jets are extremely thin and that the time needed for the tip of the jet to reach the free surface is only a small fraction of the total time from impact to cavity closure. This latter observation means that jets move much faster than the impacting solid. Indeed, as shown in the Appendix, we have experimentally measured that the ratio between the jet velocity and that of the impacting solid can reach values as high as 20. In this context, note that the impact of either a drop (Weiss & Yarin 1999; Thoroddsen 2002; Howison *et al.* 2005) or a solid object (Thoroddsen *et al.* 2004) onto a free surface also provokes the ejection of a sheet of liquid moving with a velocity of tens of times the impact velocity. More details on these types of related physical situations can be found in the review of drop impact on thin liquid layers and dry surfaces by Yarin (2006).

One of the main purposes of this paper is to explain the occurrence of Worthington jets after cavity collapse and also to provide a closed-form expression of the jet tip velocity as a function of the impactor's velocity. As a first step, we review in the next subsection the simplified model developed by Gekle *et al.* (2009*a*), as it contains the essential ingredients to understand the physics underlying the jet ejection process and since it will be used in the forthcoming sections to express the jet tip velocity as a function of the impactor's velocity.

2.3. *Reviewing the model for $r_b(t)$ and $z_b(t)$*

As pointed out above, the position of the jet base is crucial for characterizing the time evolution of liquid velocities within the jet. The first piece of evidence that clearly

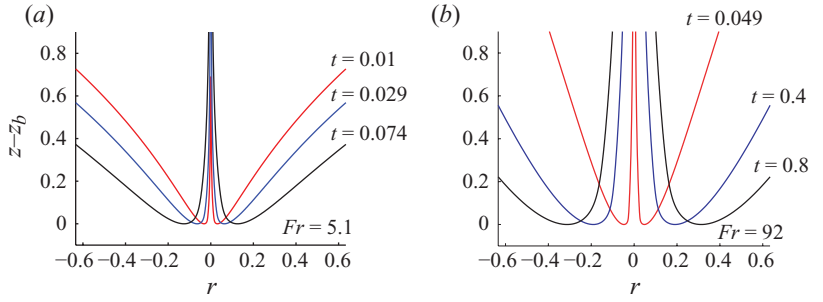

FIGURE 7. (Colour online) Jet shapes translated vertically for different instants in time and different values of the impact Froude number.

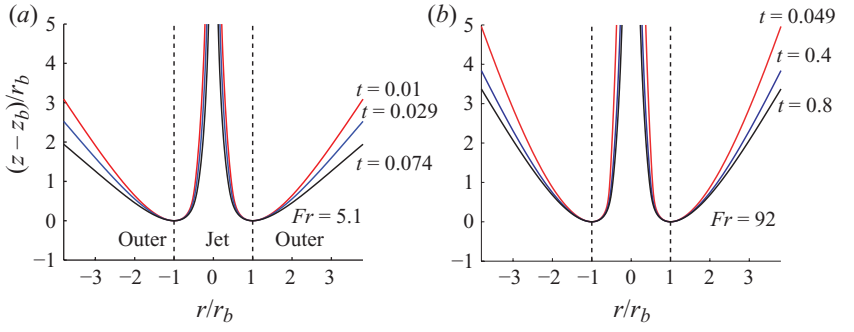

FIGURE 8. (Colour online) Shapes of the jets shown in figure 7(*a*, *b*) when distances are normalized using r_b overlay reasonably well, indicating that r_b is a good choice for the characteristic local length scale. The definition of the outer and jet regions given in § 3 is also indicated.

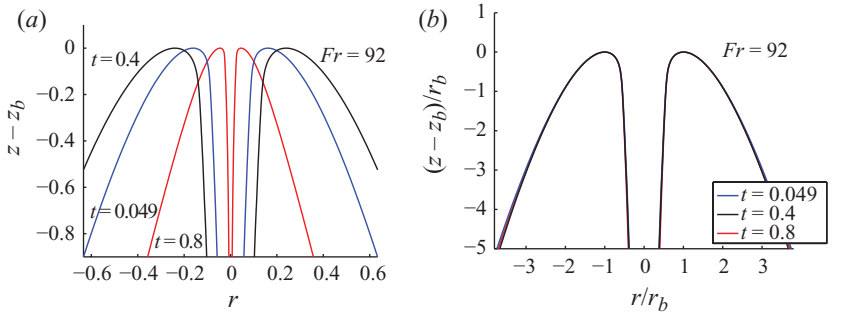

FIGURE 9. (Colour online) Jet shapes for the downward jet at $Fr = 92$, taken at the same times as in figures 7 and 8, show similarly good rescaling with the corresponding base radius r_b. Note that in (*b*) all lines overlap.

shows the importance of the radial distance r_b for the study of Worthington jets is shown in figures 7–9, where some of the different jet shapes taken from the time evolutions of figure 6 are translated vertically so that they share a common vertical origin. Note that both the jet base and the jet itself widen as the time from pinch-off increases. Interestingly enough, figures 8 and 9 show that the shapes of both the upward and downward jets exhibit some degree of self-similarity since they nearly collapse onto the same curve when distances are normalized using r_b. These figures

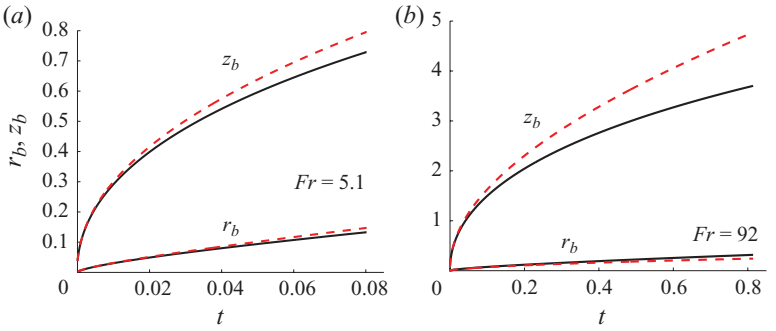

FIGURE 10. (Colour online) Time evolution of radial and axial positions of the jet base, r_b and z_b, respectively. The upward jet is shown in black (solid) and the downward jet in red (dashed) (for the downward jet $-z_b$ is shown for convenience). The behaviour of both jets is very similar.

indicate that the natural length scale for characterizing both the jet shape and the flow field within the jet is the jet base radial position, r_b.

Another length of crucial importance for describing the time evolution of the jet is the vertical distance between the pinch-off point and the jet base, namely, z_b. Figure 10 shows numerical results for the time evolutions of both r_b and z_b for two different values of the Froude number. The comparatively large values of $z_b(t)$ with respect to $r_b(t)$ are caused by the confinement of the jet by the (negative) radial velocities at the cavity interface, which partly inhibits the widening of the base radius. Note that both r_b and z_b are time-dependent length scales that do not depend on any geometrical length scale. Instead, r_b and z_b will be fixed by the dynamical local process occurring near the jet base, where the liquid is decelerated radially and is accelerated in the axial direction (Gekle *et al.* 2009*a*).

The first step in building a model to predict the time evolutions of both r_b and z_b is to find a simplified and realistic expression for the flow field in an outer region away from the jet itself ($z < z_b$ and $r > r_b$) that satisfies continuity. This will be achieved starting from Green's identity, which expresses the potential ϕ at any point $\boldsymbol{r}$ as an integral of sources and dipoles over the free surface:

$$\beta\phi(\boldsymbol{r}) = \int \frac{1}{|\boldsymbol{r}-\boldsymbol{r}'|}\frac{\partial\phi}{\partial n}\,\mathrm{d}S - \int \phi\frac{\partial}{\partial n}\frac{1}{|\boldsymbol{r}-\boldsymbol{r}'|}\,\mathrm{d}S, \tag{2.1}$$

with the integration taken over $\boldsymbol{r}'$ and $\beta = 4\pi$ in the liquid bulk. As pointed out by Gekle *et al.* (2009*a*), since the dipole term decays quickly as $1/|\boldsymbol{r}-\boldsymbol{r}'|^2$, the source term (which decays only as $1/|\boldsymbol{r}-\boldsymbol{r}'|$) will be the dominant contribution to the integral if the observation point $\boldsymbol{r}$ is chosen sufficiently far from the free surface. Taking this fact into account, in the following we will only consider the contribution coming from the source term. Moreover, we use slender-body approximation (Ashley & Landahl 1965) to write $\mathrm{d}S \simeq 2\pi r_{cav}\,\mathrm{d}z$ and $\partial\phi/\partial r \simeq \dot{r}_{cav}$, where r_{cav} and $\dot{r}_{cav}$ indicate the radius of the cavity and its associated radial velocity, respectively. This gives

$$\beta\phi = -\int \frac{2\pi r_{cav}\dot{r}_{cav}}{\sqrt{r^2+(z-z')^2}}\,\mathrm{d}z' \rightarrow 2\phi = \int \frac{q_{axis}}{\sqrt{r^2+(z-z')^2}}\,\mathrm{d}z'. \tag{2.2}$$

Thus, the starting point of our model is the description of the flow field after pinch-off using a line of sinks on the axis of symmetry of intensity $q_{axis}(z,t) = -r_{cav}(z,t)\dot{r}_{cav}(z,t)$. Both the spatial variation and the time evolution of q_{axis} are shown in figure 11. The

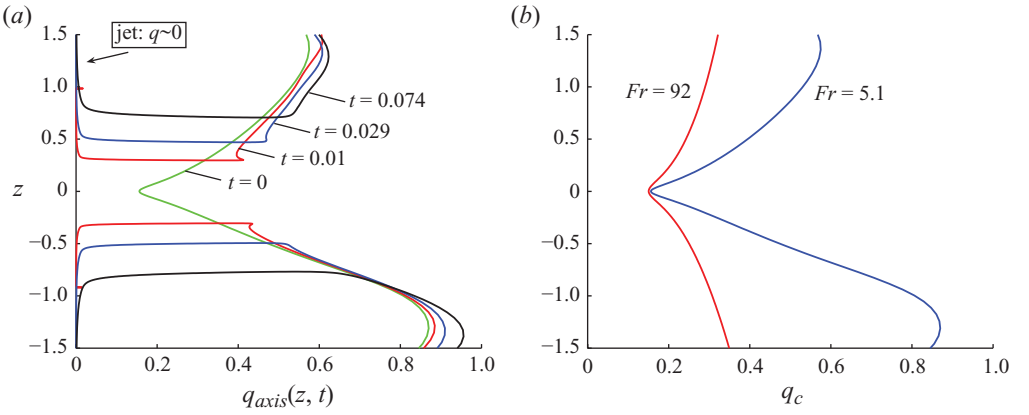

FIGURE 11. (Colour online) (*a*) The sink distribution $q_c(z) = q_{axis}(z, t = 0)$ at the moment of pinch-off (green) for the impacting disk at $Fr = 5.1$ is the essential ingredient in our jet formation model. The sink distribution on the cavity interface at later times – red, blue and black curves – remains approximately equal to the sink distribution at pinch-off (the variation during the entire time of jet formation is roughly 9 % for the upper and 2 % for the lower jet, respectively). Note that, for a given $t > 0$ and $|z| > |z_b|$, the function $q_{axis}(z, t)$ is multivalued since, for these axial positions, the interface is double-valued: the cavity and the jet (see figure 4). However, the sink strength along the jet (far left) is virtually zero due to the vanishing radial velocities at the jet interface and only the contribution of sinks along the cavity interface will be considered, i.e. $q_{axis}(z, t) = -r_{cav}\dot{r}_{cav}$. Note that the sink distribution at later times on the cavity interface can be approximated by $q_c(z)$ if two additional effects are accounted for: the accumulation of sinks around the base and the hole between the upward and the downward jets. (*b*) The sink strength distribution at the moment of pinch-off, $q_c(z)$, for two values of the Froude number.

sink distribution at pinch-off $q_c(z) = q_{axis}(z, t = 0)$ represents the central building block of our model. Note that $q_c(z)$ will depend on the Froude number, but that for clarity we will omit this dependence in the forthcoming discussion.

Figure 11 shows that the sink distribution after pinch-off along the cavity interface remains reasonably similar to the one existing right at pinch-off – except around the jet base – due to the very short time scale of jet formation. Thus, since our purpose is to develop the minimum model that retains the essential ingredients of the jet ejection process, we carry out the simplification resulting from the assumption that, along the cavity walls, the sink distribution remains constant in time and equal to the sink distribution at pinch-off, except near the jet base. Thus, the sink distribution at any instant in time can be approximated to $q_c(z)$ if two additional effects are considered: a hole is created between the bases of the upward and downward jet and sinks accumulate around the jet base (Gekle *et al.* 2009*a*). Indeed, note first that there cannot be sinks located between $z = 0$ and $z = z_b(t)$ for $t > 0$ since this would imply infinite velocities at the axis of symmetry (see figure 11). Moreover, the sink accumulation at the jet base occurs as a consequence of the 'hole' which is created between the two jet bases. Indeed, just before pinch-off occurs, the flow rate directed towards the axis is given by $Q(t = 0) = \int q_c(z')\,\mathrm{d}z'$. However, the contribution to the total flow rate of the sinks which were located at the pinch-off instant between $0 < z < z_b(t)$ namely, $\int_0^{z_b(t)} q_c(z')\,\mathrm{d}z'$ cannot disappear after pinch-off. If this happened, the value of $Q(t)$ would enormously decrease with respect to the value of Q at $t = 0$, which is physically impossible since liquid inertia prevents an abrupt time variation in Q. Consequently, the sinks that were originally located between $z = 0$ and $z = z_b$ are

rearranged and accumulated near the jet base in a typical distance $\sim O(r_b)$ in such a way that the total inward flow rate does not vary so abruptly in time. On the basis of these observations, we derived in Gekle *et al.* (2009*a*) an analytical expression for the flow potential ϕ at an arbitrary point located in the outer region. The potential is expressed as a function of the instantaneous base position $r_b(t)$, $z_b(t)$ and the sink strength at the height of the base $q_b(t) = q_c(z = z_b(t))$, which implicitly depends on time due to the motion of the jet base:

$$2\phi = \underbrace{-q_b \int_{-\infty}^{\infty} \frac{\mathrm{d}z'}{\sqrt{r^2 + (z - z')^2}}}_{\text{collapsing cavity}} + \underbrace{q_b \int_{-z_b}^{z_b} \frac{\mathrm{d}z'}{\sqrt{r^2 + (z - z')^2}}}_{\text{hole}} + \underbrace{\frac{C\, q_b\, r_b}{\sqrt{r^2 + (z - (z_b + C_{sink} r_b))^2}}}_{\text{point sink}}, \tag{2.3}$$

where the order unity constants C and C_{sink} are obtained from a fit to the numerical data. Observe that the flow field derived from the potential in (2.3) is independent of the velocities at the pinch-off location. Instead, it is clear from the expression in (2.3) that velocities in the liquid, once the cavity splits in two, are determined by the flow field induced by the collapse of the cavity interface (which keep on moving radially inwards after pinch-off) and, interestingly enough, by the local flow around the jet base induced by the point sink term. Thus, the jet ejection process is a consequence of the fact that the liquid flow field before pinch-off must be modified to account for the 'hole' which is created between $z = 0$ and $z = z_b$.

As explained by Gekle *et al.* (2009*a*), (2.3) is deduced taking into account two facts. First, note that the dominant contribution to the integral

$$I = \int_{z_b}^{\infty} q_c(z')\, \mathrm{d}z' / \sqrt{r^2 + (z - z')^2} \tag{2.4}$$

comes from the axial region closest to the observation point $\boldsymbol{r}$ and, consequently,

$$I \simeq q_c(z) \int_{z_b}^{\infty} \mathrm{d}z' / \sqrt{r^2 + (z - z')^2}\,. \tag{2.5}$$

Thus, since $\boldsymbol{r}$ will be located at an altitude z similar to or below that of the jet base, $q_c(z) \simeq q_b$ and $I \simeq q_b \int_{z_b}^{\infty} \mathrm{d}z' / \sqrt{r^2 + (z - z')^2}$. Second, note that the accumulation of sinks after pinch-off takes place near the jet base in a spatial region of typical length $\sim O(r_b)$ (see figure 11). Consequently, the contribution of these sinks to the radial inflow can be regarded as a point sink of strength $C\, r_b\, q_b$ at distances $|\boldsymbol{r}| \gg r_b$. This is because the excess of sink strength on the jet base region along the length $\sim r_b$ is, to first order, $\simeq q_b$. Moreover, the point sink will be located at the small distance above the base z_{sink}, which is proportional to the local length scale, r_b, i.e. $z_{sink} = z_b + C_{sink} \cdot r_b$.

Once an approximate expression for the potential ϕ has been deduced, the desired ordinary differential equations (ODEs) for the unknown variables $r_b(t)$ and $z_b(t)$ are obtained from both the Bernoulli equation applied at a single point on the cavity interface and the kinematic boundary condition applied at the jet base. Taking into account the fact that the liquid pressure at the cavity interface is constant and can be set to zero without loss of generality, the former equation reads

$$\frac{\partial \phi}{\partial t} + \frac{|\nabla \phi|^2}{2} = 0, \tag{2.6}$$

where the surface tension can be safely neglected because of the large value of the impact Weber number $We = \rho V_D^2 R_D / \sigma$ (see Gekle *et al.* 2009*a* for details). On the

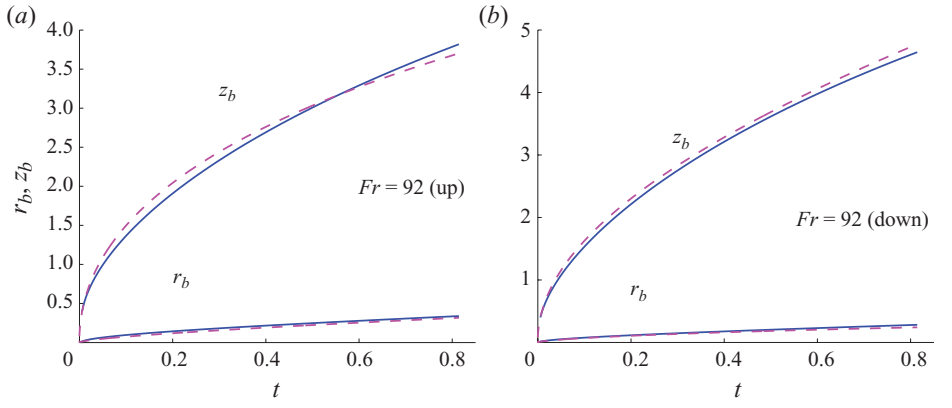

FIGURE 12. (Colour online) (*a*) Time evolution of the jet base radial and axial positions, r_b and z_b, respectively, taken from the simulation (dashed magenta lines) and the analytical model (solid blue lines) for the upward jet of an impacting disk with $Fr = 92$. The fitting constants are $C = 7.8$ and $C_{sink} = 0.63$. (*b*) The same system but for the downward jet with $C = 6.66$ and $C_{sink} = 0.55$.

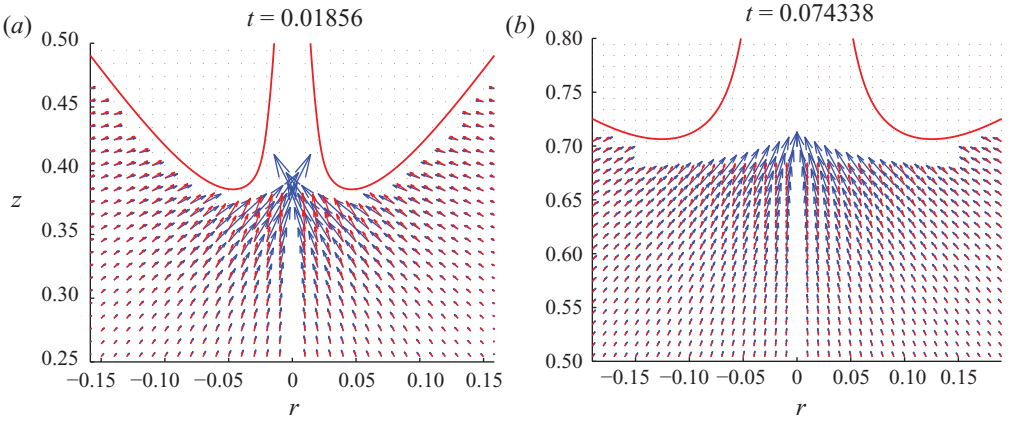

FIGURE 13. The flow field obtained from the model with $C = 4.55$ and $C_{sink} = 0.63$ for the disk impacting at $Fr = 5.1$ (blue arrows) shows fair agreement with the numerically calculated flow field (red arrows). The region inside the jet and very close around the base is excluded since the model is not perfectly reliable there (due to the assumption of the observation point far from the base).

other hand, the kinematic boundary condition is given by

$$\frac{\mathrm{d}z_b}{\mathrm{d}t} = \frac{\partial \phi}{\partial z}. \tag{2.7}$$

Note that small hydrostatic contributions have been neglected in (2.6) and, due to the fact that the jet base is a local minimum where $\partial z/\partial r = 0$, the kinematic boundary condition adopts the simple form given in (2.7).

The algebra to obtain a closed system of two ODEs from (2.6) and (2.7) is given by Gekle *et al.* (2009*a*). When the constants C and C_{sink} are appropriately fitted to reproduce the numerically obtained evolution of the jet base, not only the time evolutions of both r_b and z_b but also the entire flow field in the outer region can be reproduced with our theory. Indeed, in spite of the number of approximations, figures 5, 12 and 13 illustrate the reasonable agreement between theory and numerics, which we find in all cases studied.

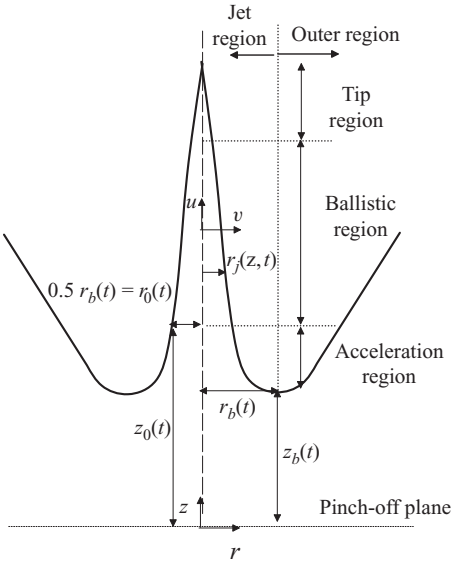

FIGURE 14. Sketch showing the different lengths used to define the jet base and the regions of the jet. The jet base (r_b, z_b) is located where the interface possesses a local minimum. The outer region covers the bulk of the fluid with $r > r_b$ and $z < z_b$. The jet region is subdivided into the acceleration, the ballistic and the tip regions. Note that, in the following, u and v will be used to denote the axial and radial velocities, respectively.

Let us remark that both r_b and z_b are calculated in terms of only the sink strength intensity at pinch-off, $q_c(z)$, once the minimum radius of the cavity, r_{min}, is fixed. In the next section we will extend this result by expressing both the jet shape and the flow field within the jet using r_b and q_b/r_b as characteristic length and velocity scales, respectively. As detailed in this section, both quantities can be expressed as a function of only q_c and r_{min}.

3. Jet structure: the flow field within the jet

The main purpose of this section is to express the velocity field within the jet as a function of the sink strength distribution at pinch-off, q_c, the radial coordinates of the jet base, r_b, and the vertical position of the jet base, z_b. Because the velocity field within the jet varies in a non-trivial manner, it proves convenient for clarity purposes to define first the different regions in which the jet is divided. As shown in figure 14, the flow is separated into two large parts: the outer region, which occupies the spatial region $r > r_b$, $z < z_b$ and has been already described by the model given in § 2.3 and the jet region, which we describe here. For that purpose, the jet region is subdivided into three subregions: the acceleration region, the ballistic region and the tip region, the latter being studied in depth in Part 2 of this paper (Gordillo & Gekle 2010).

3.1. *The acceleration region*

The acceleration region, located near the jet base, is where fluid particles are decelerated in the radial direction and accelerated upwards. This is clearly illustrated in figure 15, where both the axial and radial velocities evaluated at the jet air–liquid interface, u and v, respectively, are represented for different instants in time. In this figure one can observe that, while the axial velocities u are of similar magnitude as the radial velocities at $r = r_b$, they monotonically increase to much higher values as the

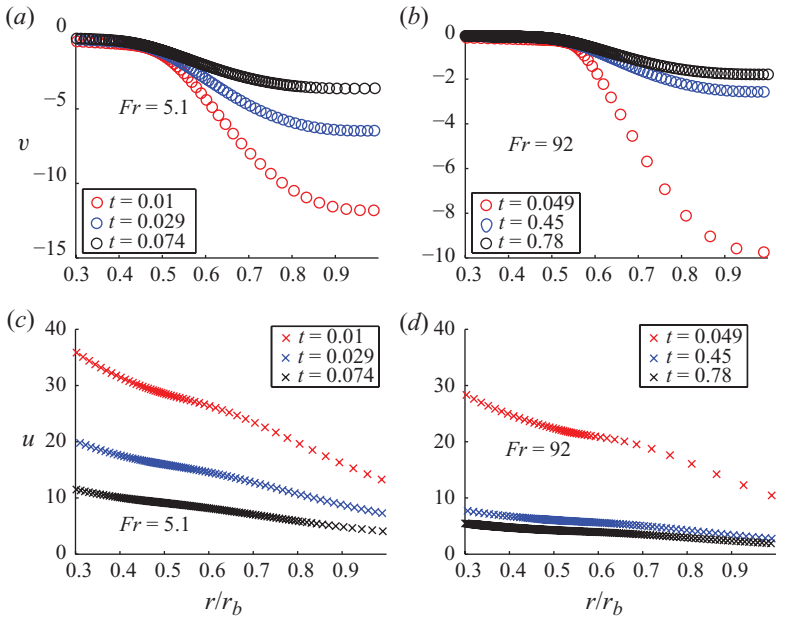

FIGURE 15. Time evolutions of the radial and axial velocities (v and u respectively) of the liquid evaluated at the jet interface for $Fr = 5.1$ (a, c) and $Fr = 92$ (b, d).

jet radius diminishes. Contrarily, the modulus of the (negative) radial velocities v decays from $\sim O(10)$ at $r = r_b$ to zero at $r \simeq 0.5\, r_b$ and, therefore, the radial inflow experiences a strong deceleration in the small distance $\sim 0.5\, r_b$. Because the liquid is at atmospheric pressure at the free surface of the jet, the strong radial deceleration provokes an overpressure below the jet base. Accordingly, a strong favourable vertical pressure gradient is created and, therefore, the liquid experiences a large upward acceleration in the vertical direction, creating the high-speed jet ejected into the atmosphere.

In view of these observations, we shall define the 'acceleration region' as the region between the base r_b and $r_0 = 0.5\, r_b$, which is the radial position on the jet interface at which radial velocities become negligible, i.e. $v \approx 0$ for jet radii smaller than r_0. The corresponding vertical position and axial velocity are denoted in what follows by z_0 and u_0, respectively. The sketch in figure 14 indicates the locations of both r_0 and z_0. All quantities to be defined in the following with the index 0 will refer to this important transition point from the acceleration into the ballistic region.

Moreover, it will prove convenient, for our purposes, to define at this point a local Weber number as $We_0(t) = \rho\, U_0(t)^2\, R_0(t)/\sigma = We\, u_0(t)^2\, r_0(t)$ (recall that capital letters indicate dimensional quantities and lower-case letters their non-dimensional counterparts). Its time evolution is depicted in figure 16. The large values indicate that surface tension effects can be neglected in the description of the jet ejection process (for a direct comparison of jet shapes with and without surface tension, see Gekle *et al.* 2009*a*).

3.2. *The ballistic region*

Because the jet interface can be considered to be at constant atmospheric pressure and surface tension effects are negligible near the jet base (cf. figure 16), the only source of axial acceleration is the axial pressure gradient caused by the radial deceleration of

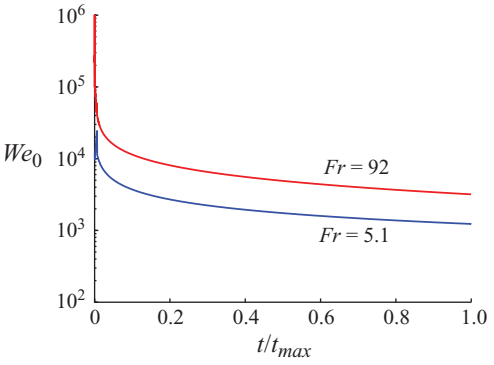

FIGURE 16. (Colour online) Time evolution of the local Weber number at the beginning of the ballistic region for two different values of the impact Froude number. The large values demonstrate that surface tension is not relevant during the jet ejection process. Here t_{max} indicates the instant at which the simulation stops.

the flow in the acceleration region. Therefore, the source of axial acceleration (radial deceleration) is no longer active high up into the jet, but only near the jet base. We will therefore define the 'ballistic region' in which no further (radial or axial) acceleration takes place and which follows at the end of the acceleration region (see figure 14).

This term is based on the fact that, since $v \simeq 0$ for $r < r_0$ and the pressure at the jet interface is atmospheric, the momentum equation projected in the axial direction yields

$$\frac{\mathrm{D}u}{\mathrm{D}t} = 0 \quad \text{for} \quad z > z_0 \quad \text{with} \quad u = u(z, t), \tag{3.1}$$

and $\mathrm{D}/\mathrm{D}t$ indicating the material derivative. In (3.1), gravitational effects have been neglected since the Froude number based on the jet radius and jet speed is always much larger than unity, i.e. $Fr\, u_0^2/r_b \gg 1$. Equation (3.1) implies that fluid particles are no longer accelerated upwards and conserve the vertical velocities they possess at $z = z_0$, which is the axial boundary between the axial acceleration region and the ballistic region. In (3.1), u is assumed not to depend on r since the radial velocity gradients of axial velocities are negligible in the ballistic region (not shown) and, thus, $u = u(z, t)$. The radius of the jet in the ballistic region, $r_j(z, t)$, is calculated from the continuity equation

$$\frac{\partial r_j^2}{\partial t} + \frac{\partial (u r_j^2)}{\partial z} = 0 \rightarrow \frac{\mathrm{D} \ln r_j^2}{\mathrm{D}t} = -\frac{\partial u}{\partial z}. \tag{3.2}$$

From the pair of equations (3.1) and (3.2), u, r_j and z_j – the height at which the jet radius is r_j – are completely determined if the relevant quantities at the beginning of the ballistic region (r_0, z_0, and the velocity u_0) are known functions of time. A particle which is ejected from the acceleration into the ballistic region at a certain time τ will move with constant velocity and thus, at a later time $t > \tau$, have attained the height

$$z_j(t) = z_0(\tau) + (t - \tau)\, u_0(\tau). \tag{3.3}$$

Therefore, because fluid particles conserve their velocities along the ballistic region of the jet, $\partial u/\partial z$ in (3.2) can be calculated as

$$\frac{\partial u}{\partial z} = \frac{\dot{u}_0(\tau)}{\dot{u}_0(\tau)(t - \tau) + \dot{z}_0(\tau) - u_0(\tau)}. \tag{3.4}$$

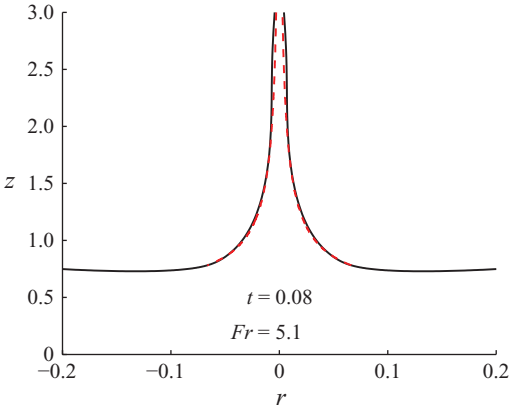

FIGURE 17. (Colour online) Comparison between the numerical jet shape and that obtained from (3.5) for the disk impact at $Fr = 5.1$. The solid black line is the simulation and the dashed red line is the analytical model. The input values of $r_0(t)$, $z_0(t)$ and $u_0(t)$ for the jet stretching model are taken from the simulations.

Thus, to obtain the corresponding jet radius r_j, (3.2) can be readily integrated to give

$$r_j^2(z = z_j, t) = r_o^2(\tau)\frac{u_o(\tau) - \mathrm{d}z_o/\mathrm{d}\tau}{u_o(\tau) - \mathrm{d}z_o/\mathrm{d}\tau - \mathrm{d}u_o(\tau)/\mathrm{d}\tau(t-\tau)}. \tag{3.5}$$

Introducing the definition of the strain rate at the beginning of the ballistic region

$$s_o(\tau) = \frac{\partial u}{\partial z}(z = z_0) = -\frac{\dot{u}_o(\tau)}{u_o(\tau) - \dot{z}_o(\tau)} \tag{3.6}$$

allows us to rewrite (3.5) in a more compact form as

$$\frac{r_j(z_j, t)}{r_o(\tau)} = \frac{1}{\sqrt{1 + (t-\tau)s_o}}. \tag{3.7}$$

Moreover, the local velocity field in a frame of reference moving at the constant velocity $u_o(\tau)$ is given by

$$u(z, t) - u_o(\tau) = \frac{s_o\, z}{1 + (t-\tau)\, s_o}, \tag{3.8}$$

where (3.6) has been substituted into (3.4) and integration over z was carried out.

Now, in order to obtain the complete jet shape at time t, we vary τ between 0 and t and use (3.3) and (3.5) to compute the corresponding vertical and radial coordinates of the jet. Note that, clearly, the particle ejected at $\tau = 0$ will end up forming the tip of the jet. The comparison between the numerical results and those obtained from the integration of the 1-D model equations (3.1)–(3.7) is depicted in figure 17. The agreement between numerics and the model further validates the approach of considering that fluid particles conserve their axial velocities within the ballistic region.

However, eventually surface tension effects will become important at the jet tip and render the above description inapplicable. The region near the tip where surface tension needs to be taken into account shall be called the 'tip region'. In this region, the jet disrupts into drops, as described in Part 2 (Gordillo & Gekle 2010).

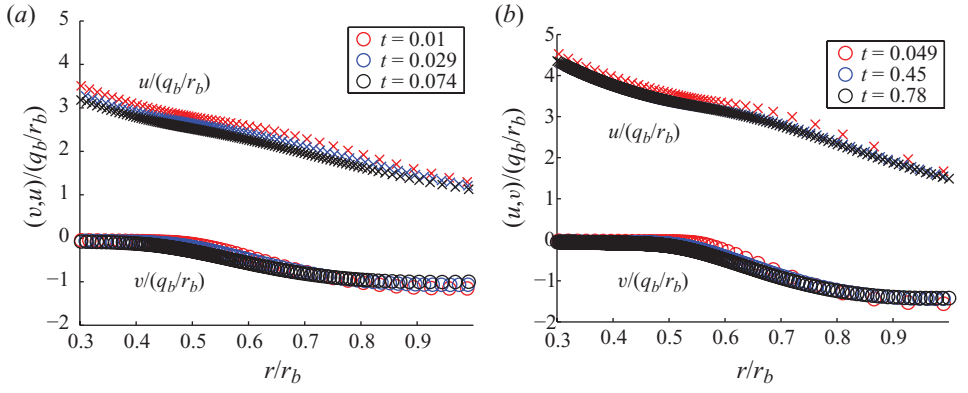

FIGURE 18. Spatial and temporal evolutions of the radial and axial velocities shown in figure 15 normalized with $q_b(t)/r_b(t)$. Observe that $u/(q_b/r_b)$ and $v/(q_b/r_b)$ nearly collapse onto the same curves for each of the two values of the impact Froude number considered, $Fr = 5.1$ (a) and $Fr = 92$ (b).

3.3. *Connecting the outer flow to the ballistic region*

Once we have shown that fluid particles conserve their velocities within the ballistic region, as a next step, we would like to link the time-dependent flow field within the jet with that existing right at pinch-off. For that purpose, we normalize the velocities v (radial) and u (axial) at the jet surface (as shown in figure 15) using, as the characteristic scale for velocities, $q_b(t)/r_b(t)$, where we recall that $q_b(t) = q_c(z = z_b(t))$ is the sink strength at the height of the jet base as described in § 2.3. The important result, shown in figure 18, is that both rescaled velocities nearly collapse onto the same master curves for a given Froude number and thus are almost constant in time for a fixed value of the rescaled position $r/r_b < 1$. This implies that, for a fixed value of q_b, axial velocities are inversely proportional to r_b, i.e. the smaller the jet base radius – or, equivalently, the more confined is the jet by the cavity interface – the larger will be the axial liquid velocities within the jet. Note that figures 8, 9 and 18 provide conclusive evidence that the correct length and velocity scales for characterizing both the jet shape and the flow field within the jet are r_b and q_b/r_b, respectively.

Of great importance for our forthcoming discussion is the rescaled axial velocity evaluated at the transition from the acceleration into the ballistic region, $B_t = u_0(t)/(q_b(t)/r_b(t))$, whose time evolution is shown in figure 19(a). In accordance with the collapse of the rescaled velocities on a single master curve shown in figure 18, B_t hardly changes with time and, thus, we can define the function $B(Fr) = u_0/(q_b/r_b)$, which also depends very weakly on the Froude number, as shown in figure 19(b).

The result in figure 19 has the additional interesting implication that axial velocities within the jet are larger than the radial velocities existing at the cavity interface before pinch-off occurs. This can be seen directly by recalling that $|q_b/r_b| = |\dot{r}_b|$ and, thus, B is the ratio between the axial velocity u_0 with which fluid is ejected into the jet and the radial inward velocity at the jet base. Then, during the initial instants of jet formation, $r_b \simeq r_{min}$, with r_{min} as the minimum radius of the cavity before the jet emerges. Therefore, because the maximum radial velocity before pinch-off occurs is $|\dot{r}_{min}| = |q_c(z = 0)/r_{min}|$, the maximum axial velocity within the jet is given by $\max(u_0) = B(Fr)\, q_c(z = 0)/r_{min} \sim 3\,\dot{r}_{min}$. This means that, essentially, the velocity

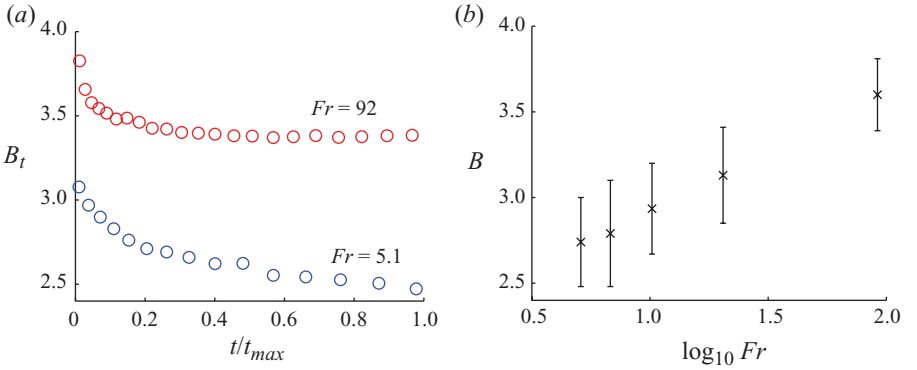

FIGURE 19. (Colour online) (*a*) The time evolution of B_t demonstrates that B_t is roughly constant in time, but does depend somewhat on the Froude number. (*b*) Taking the average of B_t over time (with error bars indicating the min/max) for different Froude numbers yields a function $B(Fr)$ which varies only between 2.5 and 3.5 in the range $3 \leqslant Fr \leqslant 92$. As indicated in figure 16, t_{max} is the time when the downward jet hits the disk and the simulation stops.

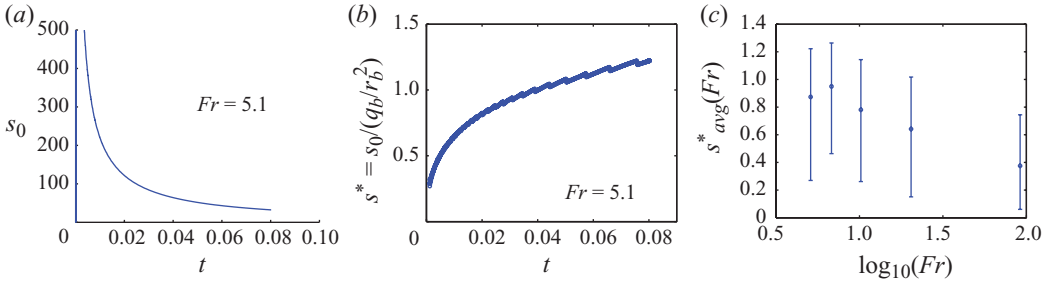

FIGURE 20. (Colour online) (*a*) Strain rate at the beginning of the ballistic region for the impacting disk. (*b*) The rescaled strain rate for the same case does not vary strongly in time. (*c*) Time-averaged values of the rescaled strain rate for different Froude numbers.

with which the jet is ejected is roughly three times larger than the maximum radial velocity attained before pinch-off.

In addition, provided that $We_0 \gg 1$, fluid particles conserve their axial velocity within the ballistic region (see (3.1)) and, consequently, the tip of the jet transports away from the pinch-off location very valuable information about the largest velocities reached during the cavity collapse process. Knowledge of the function B could thus allow an experimentalist to estimate the maximal pinch-off velocity simply from measurements of the jet tip velocity.

Figure 20 shows the value of the axial velocity gradient at the beginning of the ballistic region, $s_0 = \partial u/\partial z(z = z_0)$. Note that the values of s_0 scale with q_b/r_b^2 since, in spite of its broad variation for a fixed Froude number, the time-averaged value of $s^* = s_0/(q_b/r_b^2)$ remains of order unity during the whole evolution of the jet. Here, we provide data on s_0 because it is clear from (3.7) that s_0 determines the shape of the jet. Moreover, in Part 2 (Gordillo & Gekle 2010) it is shown that s_0 plays an essential role in the determination of both the jet breakup time and the sizes of the drops obtained.

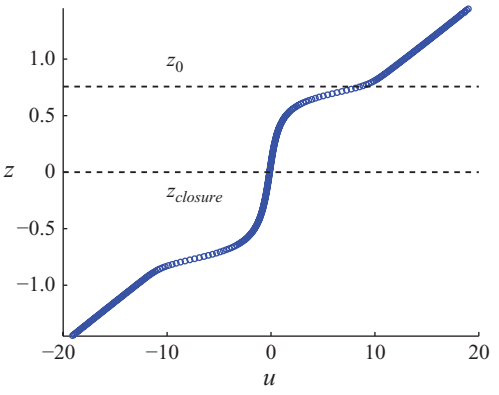

FIGURE 21. (Colour online) Vertical velocity profile for an impacting disk at $Fr = 5.1$ taken at $t = 0.074$ along the axis of symmetry shows that the flow inside the jet (above z_0) is completely disconnected from the stagnation point at $z_{closure} = 0$, which is the vertical coordinate where the cavity splits in two.

4. Comparison with a hyperbolic flow pattern

In this section we will compare the Worthington jets after solid object impact with two important results described in the literature: the hyperbolic flow patterns around a stagnation point, which have been shown to lead to jet formation in various situations, as well as the Dirichlet hyperboloids, which have been used to describe the flow pattern inside the jet itself.

At the moment of cavity collapse, the pinch-off location turns into a stagnation point: due to symmetry the radially inward-rushing fluid must be deflected vertically to form a hyperbolic flow around this stagnation point. Such a flow pattern has been inferred to be responsible for jet formation in many physical situations such as the bursting of bubbles (Boulton-Stone & Blake 1993; Duchemin *et al.* 2002; Georgescu, Achard & Canot 2002; Liger-Belair *et al.* 2008) or bubble collapse near a free surface (Blake & Gibson 1981; Longuet-Higgins 1983). In this scenario the vertical velocity would be expected to increase linearly from the stagnation point into the jet.

Figure 21 shows that we do not observe such a flow pattern in our system. Clearly, the high velocities inside the jet arise – far away from the stagnation point – in the acceleration region described in § 3.1.

Next, we will compare the flow pattern inside the jet (in the ballistic region) with the Dirichlet hyperboloids used to describe jets formed after bubble collapse near a free surface by Longuet-Higgins (1983). This theory assumes that the velocity field within the jet is a purely extensional flow of the type

$$u = \frac{\dot{A}(t)}{A(t)}\, z, \quad v = -\frac{\dot{A}(t)}{2A(t)}\, r, \tag{4.1}$$

where dots indicate time derivation and $A(t)$ is a time-dependent function which is determined by imposing that the jet free surface is at constant pressure. Making use of (3.5) and (3.8) in Longuet-Higgins (1983), the following equation for the axial strain rate $S_0 = \dot{A}/A$ can be easily derived:

$$\frac{T\dot{A}}{A} = ts_0 = \frac{T}{T_0\alpha\sqrt{1-\alpha^{-3}}}, \tag{4.2}$$

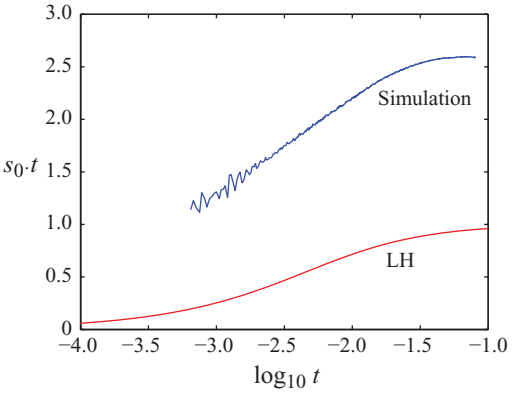

FIGURE 22. (Colour online) Comparison of the time evolution of the dimensionless strain rate $t\,s_0$ calculated using the numerical values in figure 20(*a*) (blue) with those obtained using Longuet-Higgins' theory given by (4.2) in red.

where T/T_0 is given by

$$\frac{T}{T_0} = \int_1^{\alpha} \sqrt{1-(\alpha^*)^{-3}}\,\mathrm{d}\alpha^*, \tag{4.3}$$

where α is the dimensionless counterpart of $A(t)$ and T_0 is a characteristic time, not specified in Longuet-Higgins (1983). Note that, by means of comparison with numerical results, we choose to derive here (4.2) since the quantity $t\,s_o$ does not depend on the way lengths and time are made dimensionless.

Figure 22 shows a comparison between the numerical value of $t\,s_0$, obtained from figure 20(*a*), and that predicted by (4.2) when α is varied from a value very close to 1 to around 30. This figure shows that, despite the constant T_0 being chosen to maximize the agreement of the theory in Longuet-Higgins (1983) with the numerical results, we observe that there exists a large deviation between the computed and the analytical results. The fact that the type of Worthington jets under consideration here cannot be described through the theory in Longuet-Higgins (1983) can further be appreciated in figure 23, which shows the vertical velocities within the jet as a function of the axial coordinate at two different instants in time. The acceleration region, extending from $z = z_b$ to $z = z_0$, is clearly differentiated from the ballistic region $z > z_0$. From this figure, note that $v_z = (ts_0)/tz$ – with ts_0 given by (4.2) – deviates from the numerical results despite the fact that the constant T_0 has been arbitrarily chosen to maximize the agreement with the numerics. However, the vertical velocities calculated using (3.1) with the velocity at the end of the acceleration region as initial condition is in fair agreement with the numerically computed velocities.

The reason why the theory on hyperbolic jets in Longuet-Higgins (1983) is unable to describe the type of Worthington jets studied here is because the time-dependent function $A(t)$ in (4.1) is calculated assuming that the time evolution of the flow field within the jet is determined by the flow field in the jet itself. However, as clearly shown in figure 23, the liquid velocity field within the ballistic region is imposed by the axial velocities $u_0(t)$ at the boundary z_0. Since, as discussed in the previous section, u_0 is a function of the velocity field in the outer region of the jet, the whole velocity field within the Worthington jet is determined, at each instant in time, by the flow field existing in the outer region of the jet, and not by the flow field in the jet itself.

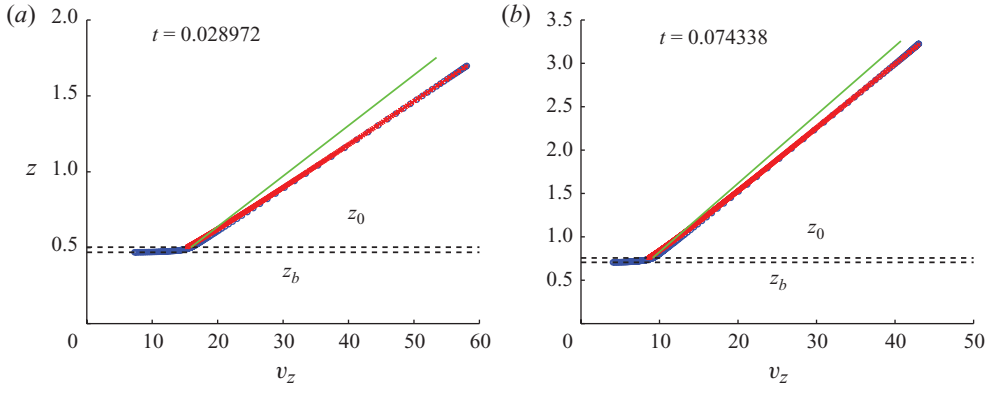

FIGURE 23. (Colour online) (a,b) Numerically computed vertical velocities (blue circles, taken on the jet surface), compared with the prediction in Longuet-Higgins (1983) (solid green line) and with the model (red crosses) presented in § 3.2, which is integrated using the values of the axial velocity u_0 at the beginning of the ballistic region, at two different instants in time. This figure shows that fluid particles conserve the velocities they possess at the end of the acceleration region.

5. Estimation of the jet shape and tip velocity using quantities before pinch-off

In this section we will show how our previous modelling efforts can be combined to yield predictions about the shape of the ejected Worthington jets as well as the jet tip velocity and, anticipating results from the accompanying paper Gordillo & Gekle (2010), the size of the first droplet ejected after jet breakup. The first prediction only requires knowledge of the cutoff radius r_{min} as well as the sink strength distribution $q_c(z)$ before pinch-off, which is obtained from the numerics as discussed in § 2.3. The second prediction about the jet tip velocity requires, next to r_{min}, only the sink strength at pinch-off at the height of closure $q_c(z=0)$. This latter quantity can be obtained from descriptions of cavity collapse available in the literature such that a complete analytical prediction is possible. Clearly, since r_{min} in our description is an imposed *ad hoc* quantity, our predictions for the velocities and the sizes of the drops in a real experiment will be accurate only if r_{min} coincides with the experimental value.

5.1. *Jet shape*

The liquid velocity field as well as the shape of the jets can be calculated by making use of only the numerical value of $q_c(z)$ and r_{min} at pinch-off (as well as the order-unity constants C and C_{sink}). The first step is to obtain the dynamics of the jet base $r_b(t)$ and $z_b(t)$ through the model in § 2.3. In the second step we use these results to calculate the axial velocity at the beginning of the ballistic region as $u_0 \simeq Bq_b/r_b$, with the sink strength at the base $q_b(t)=q_c(z_b(t))$ and B the Froude-dependent constant depicted in figure 19.

Then both the flow field and the jet shape within the ballistic region can be computed from the integration of (3.1) and (3.2) using, as initial conditions, $r_0(\tau)=0.5\,r_b(\tau)$, $u_0(\tau)=Bq_b(\tau)/r_b(\tau)$ and $z_0(\tau)=z_b(\tau)+0.5r_b$. The comparison between the jet shape calculated numerically and that obtained from the model is depicted in figure 24, and reasonable agreement is found.

5.2. *Tip velocity and drop size*

Gekle *et al.* (2009*b*) found that during the largest part of cavity collapse, the behaviour of the minimum cavity radius can be approximated by a power law with an exponent

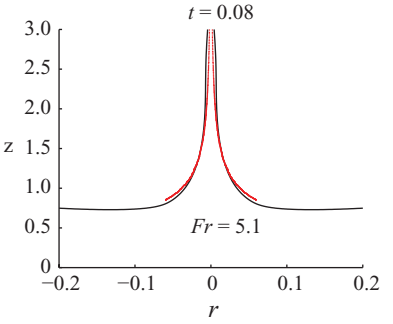

FIGURE 24. (Colour online) Comparison between the jet shape calculated using the boundary-integral code (black line) and that obtained integrating (3.1) and (3.2) using the values of r_b and z_b given by the model described in § 2.3.

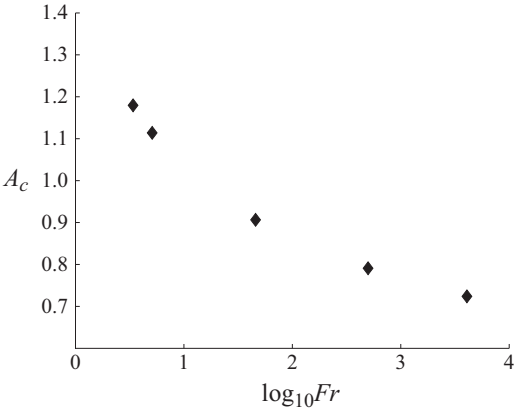

FIGURE 25. Numerical values of the function $A_c(Fr)$ in (5.1). Observe that $A_c(Fr)$ hardly varies over a range of almost four decades in Fr.

α_c that represents a time average of a time-dependent local exponent:

$$r_c = A_c(Fr)\,\tau_p^{\alpha_c} \quad \text{with} \quad \alpha_c(Fr) \simeq \frac{1}{2}\frac{\ln(K)+\ln(Fr)}{\ln(K)+\ln(Fr)-1} \to \alpha_c(Fr) > 0.5, \tag{5.1}$$

with $\tau_p = -t$ and the function $A_c(Fr)$ given in figure 25. The value of the constant K was erroneously given as $K = 0.46$ in Gekle *et al.* (2009*b*) and should correctly be $K = 66$. We note here that the precise values A_c and α_c may change when air effects (Gekle *et al.* 2010) are considered. Therefore, since the transition from the purely axisymmetric collapse to the jet ejection process occurs at $r_c = r_{min}$, the (dimensionless) sink strength at the height and moment of pinch-off is given as

$$q_c(z=0) = -r_{min}\dot{r}_{min} = A_c^{\alpha_c^{-1}}\,\alpha_c\, r_{min}^{2-\alpha_c^{-1}}. \tag{5.2}$$

We recall here that the liquid velocity at the entrance into the ballistic region is given by $u_0 = Bq_b/r_b$ and that axial velocities in the ballistic region are conserved. Furthermore, the behaviour of the jet tip is determined by the pinch-off moment where $r_b = r_{min}$ and $q_b = q_c(z=0)$. Then we can write the tip velocity V_{tip} and the

initial strain rate $S_0(t=0)$ as

$$\left.\begin{aligned} V_{tip} \sim V_D u_0 = V_D B\,\frac{q_c(z=0)}{r_{min}} \sim \frac{3\,V_D\,A_c^{\alpha_c^{-1}}\alpha_c}{r_{min}^{\alpha_c^{-1}-1}}, \\ S_0(t=0) = \frac{V_D}{R_D}\,s_0^*(t=0,Fr)\frac{q_c(z=0)}{r_{min}^2} \sim 0.5\frac{V_D}{R_D}A_c^{\alpha_c^{-1}}\alpha_c\,r_{min}^{-\alpha_c^{-1}}, \end{aligned}\right\} \tag{5.3}$$

respectively, with $\alpha_c^{-1}-1>1$ and where we have taken $B=3$ and $s_0^*(t=0)=0.5$ from figures 19 and 20.

Moreover, we have found in Gordillo & Gekle (2010) that the breakup time T_{break} and the equivalent radius of the drop ejected are given by

$$(T\,S_o)_{break} = 2.75\,We_S^{2/7} \quad \text{and} \quad R_{eq} = 0.95 R_0\,We_S^{-1/7}, \tag{5.4}$$

respectively, where $We_S = \rho\,R_0^3\,S_0^2/\sigma$ and $R_0 = 0.5\,R_D\,r_{min}$. Thus, the substitution of $S_0(t=0)$ given in (5.3) into (5.4) yields the following expressions for both the breakup time and the drop size of axisymmetric jets ejected after the impact of a circular disk:

$$\left.\begin{aligned} (T\,S_o)_{break} \sim We^{2/7}\left(A_c^{\alpha_c^{-1}}\alpha_c\,r_{min}^{-\alpha_c^{-1}}\right)^{4/7} r_{min}^{6/7}, \\ \frac{R_{drop}}{R_D} \sim 0.75 We^{-1/7}\left(A_c^{\alpha_c^{-1}}\alpha_c\,r_{min}^{-\alpha_c^{-1}}\right)^{-2/7} r_{min}^{4/7}. \end{aligned}\right\} \tag{5.5}$$

These equations constitute one of the main results of the present contribution.

6. Worthington jets observed in other systems

6.1. *Jets created from a pressure pulse*

In § 1, we enumerated a large number of physical situations which give rise to the emergence of high-speed Worthington jets out of a free surface. All of these situations share the common feature that liquid inertia dominates over viscous forces and that, for the jet to be created, there must exist a large axial pressure gradient concentrated at the spatial location where the jet is ejected. However, the origin of this axial pressure gradient differs from one physical situation to another. Let us illustrate this point using the type of purely inertial jets studied by Antkowiak *et al.* (2007), which are representative of a broader type of high-speed jets, such as those created by bubbles bursting at a free surface (Boulton-Stone & Blake 1993). In Antkowiak *et al.* (2007), it is shown that the sudden deceleration of a liquid mass creates a high-speed jet emerging out of the interface if the interface is curved. Indeed, after the liquid decelerates, the interface geometry forces the impulse pressure levels to concentrate near the surface minimum, creating large axial pressure gradients. Moreover, Antkowiak *et al.* (2007) show that the axial impulse pressure gradient is proportional to the product of the impact velocity times the aspect ratio of the cavity. Since this aspect ratio is of order unity, the ratio of the jet velocity to the impact velocity is of order unity in this type of jets. Consequently, when the impact velocity is $\sim 5\ \mathrm{m\,s^{-1}}$, Antkowiak *et al.* (2007) measure in their setup jet speeds close to $10\ \mathrm{m\,s^{-1}}$, with drop sizes of the order of 1 mm. Note also that the large impulse pressure gradient which gives rise to the emergence of the jet is created at one instant in time: just after the sudden deceleration of the liquid mass.

In our case, the axial pressure gradient is caused by the radial deceleration of the liquid which is flowing towards the axis. This process, which takes place at the jet base, creates pressure gradients of the order of $\rho V^2/(R_D\,r_b) \sim \rho V_D^2/R_D q_b^2/r_b^3$, a quantity

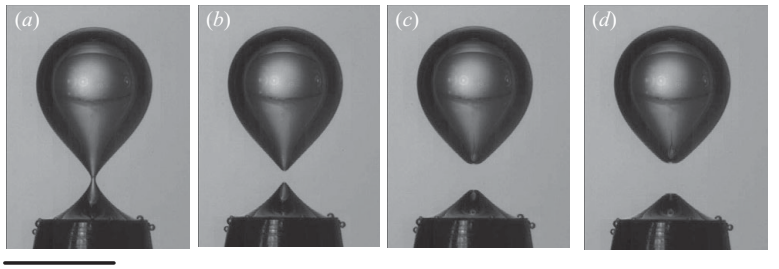

FIGURE 26. Experiment showing bubble pinch-off from an underwater nozzle. The scale bar (*a–d*) is 5 mm. Image courtesy of Rocío Bolaños-Jimenez, Alejandro Sevilla and Carlos Martínez-Bazán.

which can be huge if r_b, which is a length scale that is determined by the dynamical deceleration process as described in § 2.3, is sufficiently small. As a consequence of this, jet velocity is proportional to the impact velocity divided by a non-trivial power of the minimum radius of the cavity, as expressed in (5.3). Because of the smallness of r_{min}, jet velocities can also be of the order of 10 m s^{-1} or larger (see Appendix A), but these jet velocities can be reached with impact velocities smaller than 1 m s^{-1}. Most importantly, this pressure gradient is created continuously, while the two cavities formed after pinch-off keep on collapsing towards the axis. Note also that, since the source of pressure gradient is caused by the deceleration of a liquid mass that moves in one direction to be deflected in another direction, the type of Worthington jets studied here shares some similarities with the ejection of liquid sheets observed after the impact of drops on surfaces (see Yarin 2006 for a complete review on the subject).

6.2. *Jet ejection after bubble pinch-off from an underwater nozzle*

There is a physical situation (besides solid-body impact) which can be described using the results of the previous sections. Indeed, the type of Wortington jets created after the pinch-off of a bubble from an underwater nozzle, a process which is illustrated in figure 26, shares many similarities with the case studied in the previous section. In this case, air is injected into a stagnant liquid pool and a bubble starts to grow from the nozzle end. Then, buoyancy makes the bubble rise, elongating its neck, and when the bubble volume reaches the critical (Fritz) volume, capillarity will cause the pinch-off of the bubble (Longuet-Higgins *et al.* 1991; Oguz & Prosperetti 1993; Burton *et al.* 2005; Keim *et al.* 2006; Gordillo *et al.* 2007; Thoroddsen *et al.* 2007*a*, 2008; Bolanos-Jiménez *et al.* 2008; Burton & Taborek 2008; Gordillo 2008; Schmidt *et al.* 2009). Figure 26 shows that, as a consequence of bubble pinch-off, a jet shoots upwards from the pinch-off location. Since these jets also arise as a result of the collapse of a cavity, we shall show next that they are very similar in nature to the Worthington jets observed after solid object impact.

To simulate this system numerically, the potential flow approach will also be applied. This simplification is justified in view of the results of Oguz & Prosperetti (1993) and Bolanos-Jiménez *et al.* (2008), who show that, down to length scales of the order of 10 μm, both boundary-integral simulations and the inviscid theory of Gordillo (2008) reproduce the experiments. In this case, the minimum radius will also be fixed to $r_{min} = 0.01$ and, again, the cutoff radius will be relevant only for the tip region of the jet, as discussed at length in Appendix A. Here, distances are made non-dimensional using the nozzle radius R_N as the characteristic length scale; moreover,

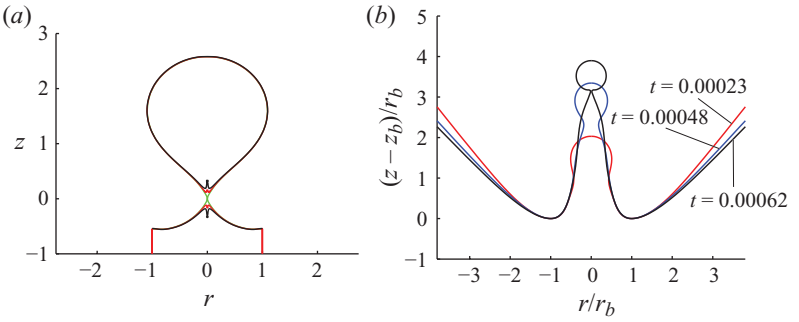

FIGURE 27. (Colour online) (*a*) Time evolution of jets formed after the collapse of gas bubbles injected into a quiescent liquid pool through a nozzle (red line), showing the ejection of the first drop, for $Bo = 2.1$. (*b*) The shapes show good overlap when distances are normalized using r_b.

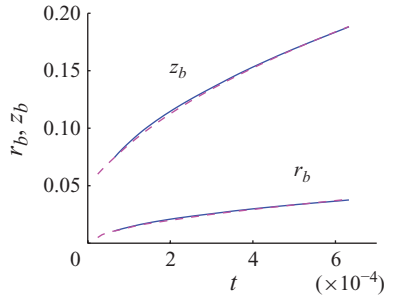

FIGURE 28. (Colour online) Dynamics of the jet base after the pinch-off of an air bubble grown from an underwater nozzle. The model with $C = 4$ and $C_{sink} = 0.61$ (solid blue line) reproduces very well the numerical results (dashed magenta line) shown in figure 27.

the prescribed gas flow rate Q_g is used to derive the typical time scale $T_N = (\pi R_N^3)/Q_g$. For the quasi-static injection conditions considered here, the relevant dimensionless parameter characterizing this physical situation is the Bond number $Bo = \rho R_N^2 g/\sigma$ (Longuet-Higgins *et al.* 1991; Oguz & Prosperetti 1993; Bolanos-Jiménez *et al.* 2008), which in the case presented here is $Bo = 2.1$. More details of our simulation method are given in Appendix B and in Gekle *et al.* (2009*b*).

In order to check whether these types of jet are describable using the results of the previous sections, we first check if r_b is the relevant length scale of the problem. Figure 27(*b*) shows that, indeed, the different shapes nearly collapse onto the same master curve when distances are normalized using r_b. Further evidence indicating that these jets are similar in nature to those ejected after solid-body impact is depicted in figure 28, where the time evolutions of both r_b and z_b calculated using the model reviewed in § 2.3 are compared with the numerical results extracted from figure 27.

In fact, the only difference between these jets and those described in the previous sections is depicted in figure 29(*a*): in the present case, the local Weber number evaluated at the beginning of the ballistic region is $\sim O(10)$, whereas in the case of Worthington jets ejected after the impact of a solid body against a free surface, $We_0 \gtrsim 10^3$. As a consequence of this, the total length at breakup of the jets ejected after bubble pinch-off is $\sim O(10r_b)$ (see figure 27*b*), i.e. much shorter than the length of the Worthington jets in § 3.

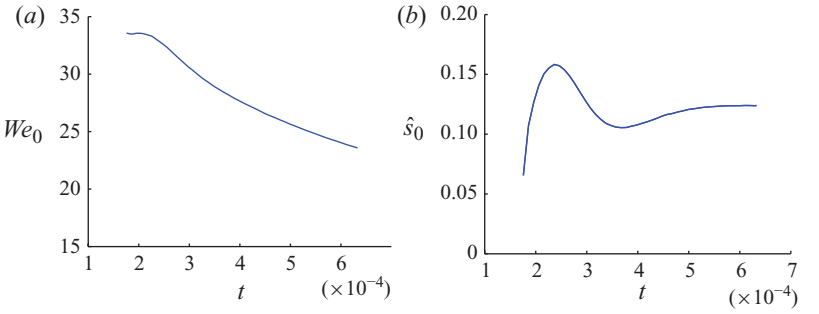

FIGURE 29. (Colour online) (*a*) Time evolution of the local Weber number for the jet shown in figure 27. (*b*) Time evolution of the normalized strain rate $\hat{s}_0 = s_0/(u_0/r_0)$ at the beginning of the ballistic region for the same case as in (*a*).

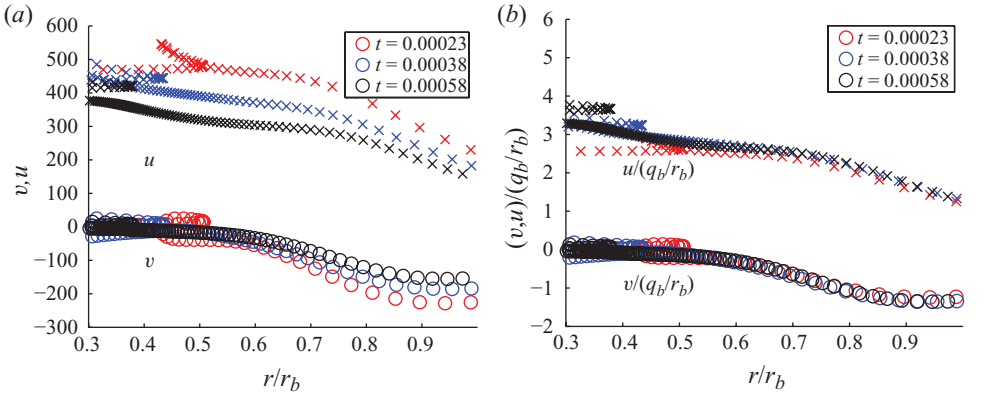

FIGURE 30. (*a*) Axial and radial velocities evaluated at the jet interface for the case shown in figure 27. In analogy with figure 18, both the acceleration and ballistic regions are clearly identified: the modulus of the radial velocities decreases from $r = r_b$ to become negligibly small for $r/r_b \lesssim 0.5$. (*b*) The same as in (*a*), but with velocities scaled with q_b/r_b. Because the Weber number is considerably smaller in this case than for the impacting disk, the jet tip region can be seen in this figure as the multivalued part of the curves u and v for $r/r_b \simeq 0.4$.

Such comparatively low values of the local Weber number indicate that surface tension must have an effect in the description of the jet. This is clearly shown in figure 30, where the collapse onto each other of the normalized time evolutions of the axial and radial velocity components evaluated at the free surface (u and v respectively) is also somewhat deteriorated when compared with the case shown in figure 18. Nevertheless, the acceleration and ballistic regions are clearly differentiated in figure 30 and, in addition, the normalization of the interfacial velocities with q_b/r_b leads to a reasonable collapse onto a single master curve (see figure 30). Consequently, since the ballistic region is also present in these types of jets, it is expected that the model developed in § 3.2 for the jet shape is also applicable to this case, which is confirmed in figure 31.

Finally, we define – in analogy to the case of the impacting disk – the ratio between the velocity at the end of the acceleration region u_0 and the typical velocity at the base q_b/r_b as the function $B(t) = u_0/(q_b/r_b)$. As shown in figure 32(*a*), the averaged value of $B(t)$ is around $B \approx 2.7$, similar to the case of the impacting disk. Finally, we

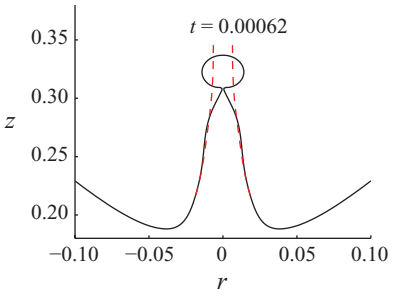

FIGURE 31. (Colour online) Comparison between the numerical jet shape and that obtained from (3.5) for the jet ejected from the underwater nozzle depicted in figure 27(*b*). The solid black line is the simulation and the dashed red line is the analytical model. The input values of $r_0(t)$, $z_0(t)$ and $u_0(t)$ for the jet stretching model are taken from the simulations. Note that since surface tension is not included in this model, the tip of the jet requires a separate treatment as described in Part 2 (Gordillo & Gekle 2010).

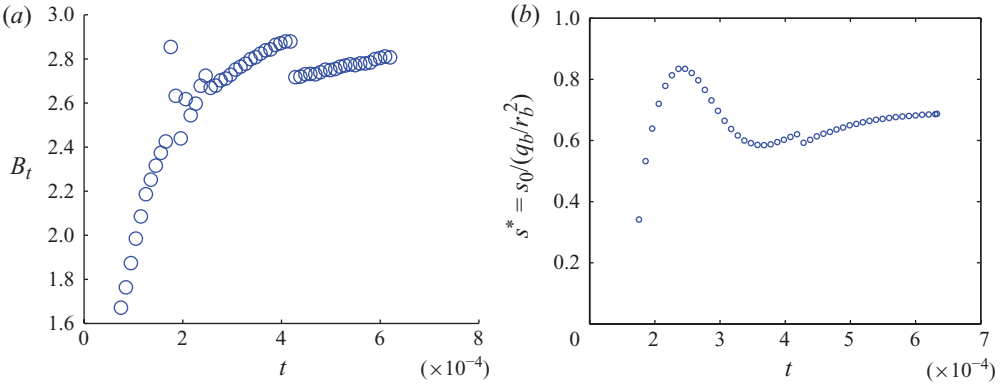

FIGURE 32. (Colour online) (*a*) The rescaled velocity at the end of the acceleration region for the underwater nozzle shows similar values as for the impacting disk in figure 19. (*b*) The rescaled strain rate is similar in both cases.

show in figure 32(*b*) the function s^* defined in figure 20 which again shows similar values for both systems.

6.2.1. *Estimation of tip velocity of jets formed after bubble collapse using quantities before pinch-off*

It is our purpose here to extend the analysis of § 5 to predict the jet tip velocity as well as the sizes of the drops obtained after bubble pinch-off as a function of the nozzle size and the material properties of the liquid. In order to take advantage of the expressions for V_{tip} and S_0 in (5.3), we have integrated the pair of equations in Gordillo (2008) using, as initial conditions, the experimental data given in Bolanos-Jiménez *et al.* (2008). Then, we have expressed the time evolution of the minimum radius of the bubble as $r_b = A_b \tau_p^{\alpha_b}$. In this case, both A_b and α_b depend on the two dimensionless parameters characterizing this physical situation namely, the Bond number Bo and the Weber number based on the gas flow rate Q_g, $We_Q = \rho Q_g^2/(\pi\sigma R_N^3)$. Nevertheless, the values of We_Q in the experiments of

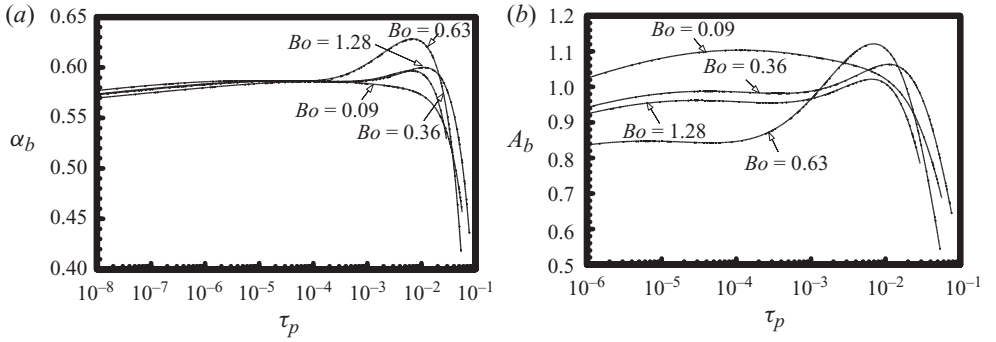

FIGURE 33. Numerical values of the functions $\alpha_b(Bo)$ (*a*) and $A_b(Bo)$ (*b*) when the integration of the pair of 2-D Rayleigh-like equations in Gordillo (2008) with the initial conditions given by the experimental data in Bolanos-Jiménez *et al.* (2008) is adjusted to a function of the type $r_b(\tau_p) = A_b(Bo)\tau_p^{\alpha_b(Bo)}$. Observe that $\alpha_b(Bo)$ hardly varies with Bo and τ_p and thus that $\alpha_b(Bo) \simeq 0.575$ is a good approximation for the whole range of Bo and τ_p considered. However, A_b slightly varies with Bo and τ_p and reasonable approximations to this function are $A(Bo = 0.09) \simeq 1.05$, $A(Bo = 0.36) \simeq 0.98$, $A(Bo = 0.63) \simeq 0.85$, $A(Bo = 1.28) \simeq 0.96$.

Bolanos-Jiménez *et al.* (2008) are so small that A_b and α_b are expected to depend significatively only on Bo and on time, as depicted in figure 33. However, from this figure note also that good approximations for both α_b and A_b are $\alpha_b \simeq 0.575$, with relative errors of $\sim 2\,\%$ and $A_b \simeq 1$, with relative errors of the order of $10\,\%$. Therefore, since in this case velocities are made dimensionless using the capillary velocity $V_c = (\sigma/\rho\, R_N)^{1/2}$, both V_{tip} and S_0 can be expressed as

$$\left.\begin{aligned} V_{tip} &\sim 1.5 \left(\frac{\sigma}{\rho R_N}\right)^{1/2} A_b^{\alpha_b^{-1}} \alpha_b\, r_{min}^{1-\alpha_b^{-1}}, \\ S_0(t=0) &\sim 0.5 \left(\frac{\sigma}{\rho R_N^3}\right)^{1/2} A_b^{\alpha_b^{-1}} \alpha_b\, r_{min}^{-\alpha_b^{-1}}. \end{aligned}\right\} \tag{6.1}$$

Thus, similar to the case of the impacting disk considered in § 5, the breakup time and the size of the drops can be approximated by

$$\left.\begin{aligned} (T S_o)_{break} &\sim \left(A_b^{\alpha_b^{-1}} \alpha_b\, r_{min}^{-\alpha_b^{-1}}\right)^{4/7} r_{min}^{6/7}, \\ \frac{R_{drop}}{R_N} &\sim 0.75 \left(A_b^{\alpha_b^{-1}} \alpha_b\, r_{min}^{-\alpha_b^{-1}}\right)^{-2/7} r_{min}^{4/7}. \end{aligned}\right\} \tag{6.2}$$

7. Conclusions

Using detailed boundary-integral simulations together with analytical modelling, we have studied the formation and breakup of the high-speed Worthington jets ejected either after the impact of a solid object on a liquid surface or after the pinch-off of a gas bubble from an underwater nozzle. To describe the phenomenon as a whole we divided the flow structure in two parts separated by the jet base (r_b, z_b): the outer region for $r > r_b$, $z < z_b$ and the jet region, extending from the jet base to the axis, i.e. $r < r_b$ and $z \geqslant z_b$. The jet region is further divided into three subregions: the axial acceleration region, where the radial inflow induced by the cavity collapse is decelerated radially and accelerated axially; the ballistic region, where fluid particles are no longer accelerated vertically and thus conserve the axial momentum they

possess at the end of the acceleration region; and the tip region, where the jet breakup process occurs.

The axial acceleration region of characteristic length $O(r_b) \ll z_b$ is where the fluid is decelerated in the radial direction, which causes an overpressure that accelerates the fluid vertically. Hence this is a very narrow region, localized near the jet base, of crucial importance for the jet ejection process since it is where the fluid particles transform their radial momentum into axial momentum. We have found the important result that both radial (v) and axial (u) velocities, when normalized with $q_c(z=z_b)/r_b(t) = q_b(t)/r_b(t)$, with $q_c(z)$ as the sink distribution at pinch-off, nearly collapse onto the same master curves for both the disk and the underwater nozzle. Therefore, the values of the rescaled velocities $(u, v)/(q_b/r_b)$ are almost constant in time for a fixed value of the rescaled position $r/r_b < 1$. We have also found that $v/(q_b/r_b) \simeq 0$ for that part of the jet surface whose radius is smaller than $r_0 = 0.5\, r_b$. Therefore, since the source of axial acceleration – radial deceleration of the fluid – is no longer active when $r < r_0$, the corresponding vertical position z_0 constitutes the upper boundary of the acceleration region.

In the slender ballistic region both the axial and radial pressure gradients are negligible since $v \simeq 0$ and surface tension forces can be neglected. Therefore, we have developed a 1-D model assuming that fluid particles conserve their vertical velocities along the ballistic portion of the jet that accurately predicts both the shape and the velocity of the jet calculated numerically. A consequence of the fact that fluid particles are not accelerated in the ballistic region is that these types of jets cannot be described using the theory by Longuet-Higgins (1983), which is based on the assumption that the flow field within the jet is a purely axial straining flow.

Most interestingly, since we have linked the flow within the jet with the sink distribution at pinch-off, we provide closed-form expressions for the velocities and the sizes of the drops obtained as a function of the radius of the impactor R_D, the impactor's speed V_D and the cutoff radius r_{min} at which the topological transition between the continuous cavity into two separate cavities occur. The expressions for the jet tip velocity in (5.3) and (6.1) reveal that the large velocities usually encountered in these systems are intimately related to the smallness of r_{min}, which is the minimum length scale at which the radial inertia of the liquid can be focused. Moreover, the results obtained for Worthington jets ejected after solid impact on a free surface have been extended to the case of jets generated after bubble pinch-off from an underwater nozzle.

In summary, our modelling of Worthington jets allows one to predict the jet base dynamics, the jet shape, and even the size of the ejected droplets based only on the knowledge of quantities before pinch-off.

We gratefully acknowledge many helpful discussions with Devaraj van der Meer and Detlef Lohse; Alejandro Sevilla and Carlos Martínez-Bazán are also acknowledged for valuable comments. We further thank Johanna Bos for providing the experimental data for the jet base and Arjan van der Bos, Oscar Enríquez and Ivo Peters for the experimental photographs. We are also grateful to Rocío Bolaños-Jiménez for her experimental images shown in figure 26. We would also like to thank Francisco del Campo-Cortés for the experiments depicted in figures 37 and 38. J.M.G. is grateful for financial support by the Spanish Ministry of Education under Project DPI2008-06624-C03-01. S.G.'s contribution is part of the programme of the Stichting FOM, which is financially supported by NWO.

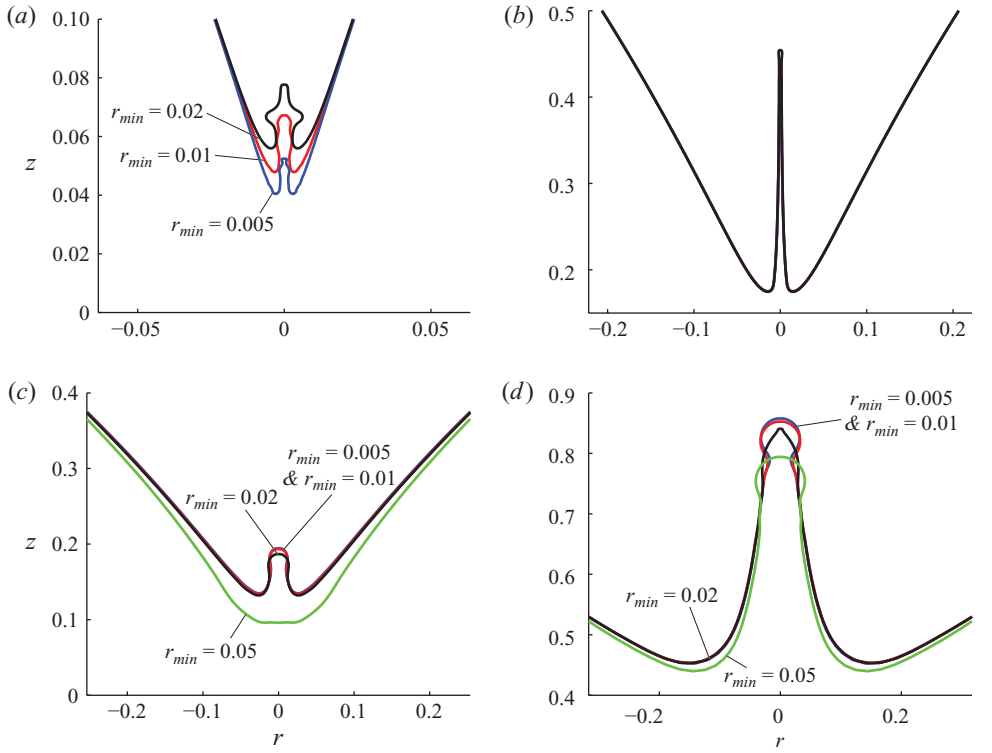

FIGURE 34. (Colour online) (*a*, *b*) Jet shapes for the disk impact at $Fr = 5.1$ at two different instants in time, $t = 10^{-4}$ (*a*) and $t = 3.2 \times 10^{-3}$ (*b*), for three different values of the cutoff radius, $r_{min} = 0.005$ (blue), $r_{min} = 0.01$ (red) and $r_{min} = 0.02$ (black). Note that in (*b*) all three lines overlap. It is evident that the effect of varying the cutoff is significant only in the very first instants after pinch-off and at the very tip of the jet. (*c*, *d*) Jet shapes for the underwater nozzle at $t = 0.0003$ (*c*) and $t = 0.004$ (*d*) (here the simulations are extended beyond the ejection of the first droplet) for four different values of the cutoff radius, $r_{min} = 0.005$ (blue), $r_{min} = 0.01$ (red), $r_{min} = 0.02$ (black) and $r_{min} = 0.05$ (green). The Bond number in the simulations is $Bo = \rho g R_N^2/\sigma = 2.1$.

Appendix A. The cutoff radius r_{min} and its relation with azimuthal distortions

As numerically simulated Worthington jets are formed after the closure (pinch-off) of the cavity, it seems natural that the cutoff radius at which the topological transition from the cavity collapse to the disjoint collapse is imposed should play an important role in the subsequent formation of the jet. However, as we have shown in Gekle *et al.* (2009*a*), the velocity field in the largest part of the jet is determined only by the local flow around the jet base and not by the pinch-off singularity. We show here that, except for the very tip, the evolution of the jet can be well described without a precise knowledge of the cutoff radius r_{min}. Indeed, in order to show that the present axisymmetric simulations are able to describe the real jet, we have decided to numerically vary r_{min} within reasonable bounds and to analyse carefully this effect on the subsequent time evolution of the jet. It can be clearly seen in figure 34 that differences in the simulations can be observed in both the jet base and tip region just after pinch-off occurs. However, as soon as the jet radius at its base becomes of the order of the maximum value of r_{min} explored, differences in the jet base region

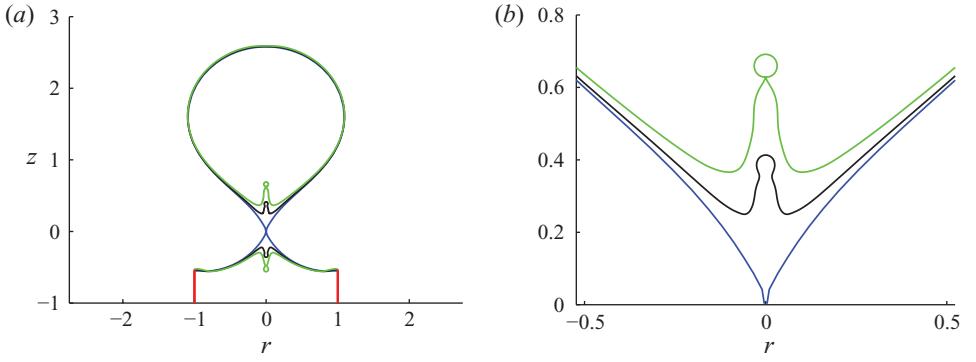

FIGURE 35. (Colour online) (*a*) Time evolution of jets formed after the collapse of gas bubbles injected into a quiescent liquid pool through a nozzle (red line) when $r_{min} = 0.05$, showing the ejection of the first drop. (*b*) A close-up of the jet region in (*a*). The colours correspond to different dimensionless times: $t = 0$ (blue/grey), $t = 0.0014$ (black) and $t = 0.0027$ (green/light grey). $Bo = 2.1$.

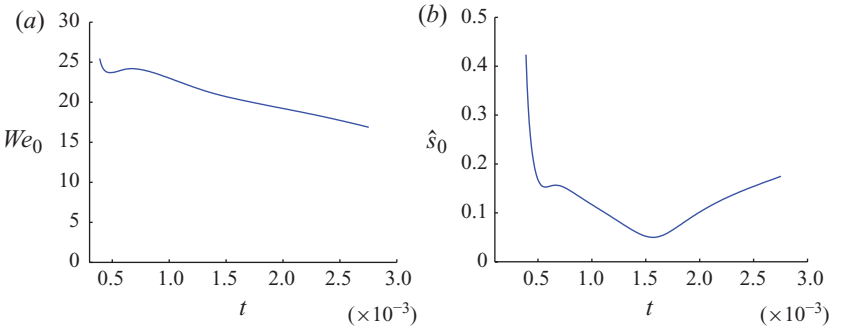

FIGURE 36. (Colour online) (*a*) Time evolution of the local Weber number for the jet shown in figure 35. (*b*) Time evolution of the normalized strain rate $\hat{s}_0 = s_0/(u_0/r_0)$ at the beginning of the ballistic region for the same case as in (*a*).

disappear and only remain appreciable in the jet tip region. Physically, this means that the effect of varying r_{min} will only be felt at the highest part of the jet, which represents only a very small fraction of both the total volume and the total kinetic energy of the jet.

However, (5.3) and (6.1) show that the value of r_{min} does influence the jet tip velocity. This is illustrated in figures 35 and 36, where it is shown that the Weber number of the jet is noticeably smaller when $r_{min} = 0.05$ than when $r_{min} = 0.01$ (see figure 29). Note that the results in figures 29 and 36 imply that, since the jet radius of curvature at the tip increases with r_{min}, the jet tip velocity increases when r_{min} decreases.

Experimentally, the velocity at which the jet is ejected strongly varies from one experiment to another and this is due to the fact that, in a real situation, there also exists an unknown cutoff radius. Indeed, besides effects such as air flow (Gordillo *et al.* 2005, 2007; Gekle *et al.* 2010), asymmetries influence the radial flow focusing effect on the central axis even before the actual cavity closure (Burton *et al.* 2005; Bartolo *et al.* 2006; Keim *et al.* 2006; Schmidt *et al.* 2009; Turitsyn, Lai & Zhang 2009). Thus, azimuthal distortions triggered by the gas shear (Leppinen & Lister 2003) or geometrical asymmetries (neither of them captured by our axisymmetric simulations)

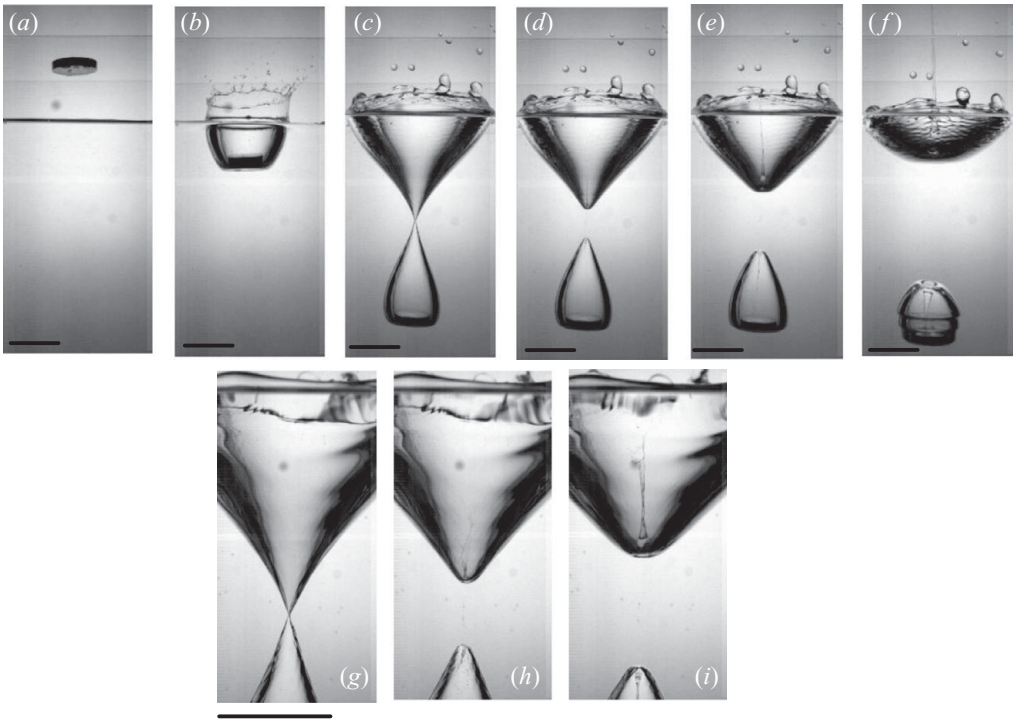

FIGURE 37. (*a–i*) Smooth cavity formed after the normal impact of a polished brass disk with sharp edges against a water interface. The disk, 22 mm in diameter and 4.7 mm in height, weighs 14×10^{-3} kg. The trajectory of the disk is forced by letting the disk fall by gravity inside a wet tube – with an internal diameter only slightly larger than that of the disk – which is aligned vertically. This forces the impact to be very nearly perpendicular to the interface. The impact velocity is $V_{impact} = 1.5$ m s^{-1}. The time lapse between the different frames with respect to the impact time is -15, 14, 86.08, 86.71, 88.49 and 98.34 ms. Note that, while the time between impact and cavity closure is roughly 85 ms, the upward jet reaches the free surface in less than 3 ms, indicating that the jet velocity is much larger than the impactor's velocity. Indeed, the initial velocity of the tip of the jet, measured from detailed images of the type in (*g–i*), is larger than 18 m s^{-1} and thus larger than 10 times the disk velocity. The huge velocities reached by the liquid jet can also be seen by a comparison with the velocity of the drops formed in the corona splash which hardly change their position between the third and sixth frames. Note that the initial impact dynamics could be influenced by the fact that the surface of the brass disk is wet. The scale bar is 22 mm.

lead to a decrease of the liquid acceleration towards the axis before pinch-off, reducing the speed of the ejected jet, which is thus fixed when azimuthal asymmetries become of the order of the minimum radius of the cavity. Because the amplitude of these tiny asymmetries is almost impossible to control, the jet tip velocity will vary from one experiment to another.

For the purpose of illustrating the previous assertion, figures 37 and 38 show the cavity formation and jet ejection processes when either a brass disk (smooth surface) or a golf ball (structured surface) impact perpendicularly on a quiescent pool of water. Despite the fact that both the velocity and the diameter of the ball are larger than those of the disk, the maximum jet velocity is larger for the disk case. Indeed, while the shape of the cavity in figure 37 is smooth, the cavity interface in figure 38 clearly already exhibits asymmetric modulations just after the impact (which – in addition to the rough surface structure – may in part also be due to a rotation of

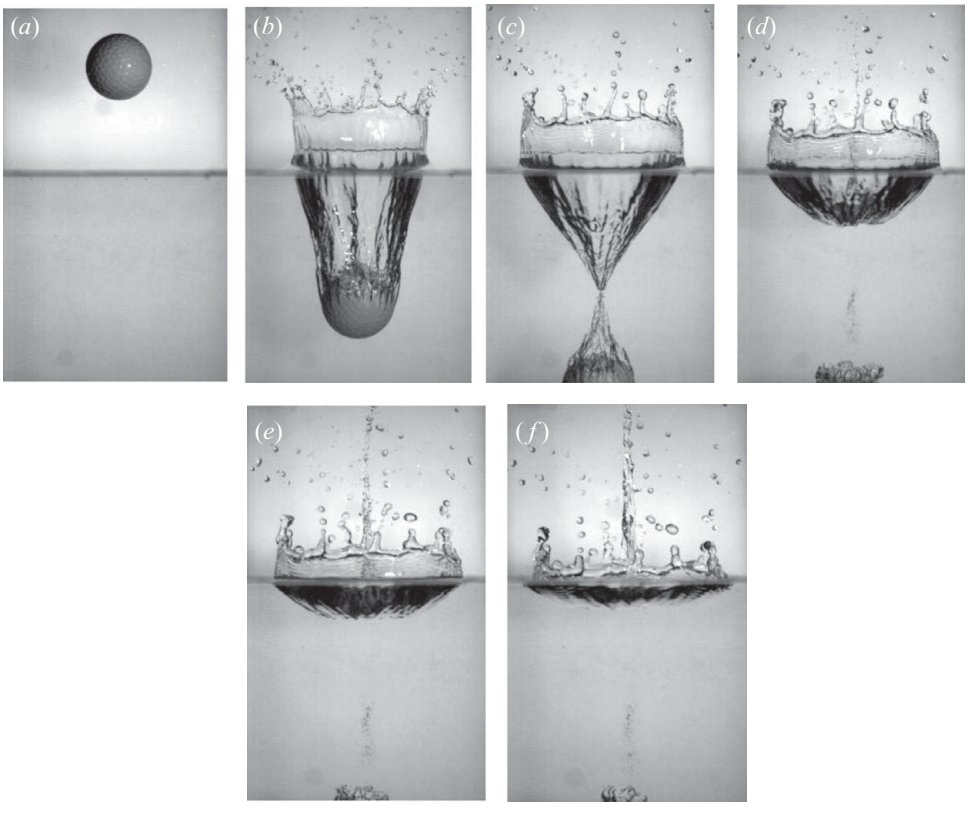

FIGURE 38. (*a–f*) Cavity formation caused by a golf ball with a diameter of 42.75 mm and a mass of 46.5×10^{-3} kg impacting with a velocity of 2.3 m s^{-1}. Compared with figure 37 the surface shape is visibly distorted due to the rough surface structure of the ball. Nevertheless, it can be inferred from a detailed image analysis that the jet velocity is again much larger than the ball's velocity. However, in spite of both the impact velocity and the ball diameter being larger than those of the disk, the maximum velocity of the jet is only $V_{tip} \simeq 17.5$ m s^{-1} and thus, the ratio between the jet speed and the impact speed is smaller than that for the disk.

the ball). Consequently, since the self-acceleration of the liquid towards the axis is lost when the amplitude of azimuthal disturbances is similar to the radius of the cavity, the maximum velocity reached during the collapse process decreases when the cavity interface is not smooth. Note that figures 37 and 38 are representative of an exhaustive set of experiments. The analysis of the whole experimental data has shown that the tip velocity varied from one experiment to another for both the golf ball and the disk. However, on average, the largest jet speeds are measured when throwing the disk.

Therefore, we can conclude that although the jet tip is where the highest velocities are reached, it is also the least reproducible one from an experimental point of view since it strongly depends on the precise details of pinch-off. Thus, regarding experimental reproducibility, our study will be valid for accurate description of the most robust part of the jet. As emphasized above, this is because the flow within the jet – except at its tip – is not determined by the velocity field at the pinch-off location, but by the time-dependent local flow field surrounding the jet base (Gekle *et al.* 2009*a*).

Appendix B. Numerical methods

In this paper we have used two types of boundary-integral simulations which model the normal impact of a disk on a free surface (see § 3) and the pinch-off of a bubble from an underwater nozzle, respectively (see § 6.2).

B.1. *Disk impact simulations*

The numerical calculations are performed using an axisymmetric boundary-integral method as described by Bergmann *et al.* (2009). As the dynamics of air (Gekle *et al.* 2010; Gekle & Gordillo 2010) only negligibly influences the jet, we choose to run single-phase simulations, neglecting the influence of the air.

Our simulations are based on describing the velocity field as the gradient of a scalar potential. In the axisymmetric geometry the surface integrals arising in the boundary-integral formulation reduce to 1-D line integrals (Oguz & Prosperetti 1993; Pozrikidis 1997) which are evaluated with eight-point Gaussian quadrature. Known quantities, i.e. the flow potential ϕ over the free surface and its normal derivative ϕ_n over the disk, are interpolated using cubic splines, while for the unknown quantities linear interpolation is used. The discretization of the boundary-integral equation using collocation results in a linear system of equations which is solved by LU decomposition.

The time evolution of the free surface is given by the kinematic and dynamic boundary conditions

$$\frac{\mathrm{d}\boldsymbol{r}}{\mathrm{d}t} = \boldsymbol{v} \tag{B 1}$$

and

$$\frac{\mathrm{D}\phi}{\mathrm{D}t} = \frac{1}{2}|\boldsymbol{v}|^2 - Fr^{-1}z - We^{-1}\kappa, \tag{B 2}$$

respectively, with κ as the local curvature of the surface and the other quantities as defined in the main text. For time stepping, an iterative, second-order accurate Crank–Nicolson scheme is employed with time steps determined by the condition that neighbouring nodes may not 'cross', i.e.

$$\Delta t = f \min(t_{node}) \tag{B 3}$$

with $t_{node} = D/v_{node}$, where D is the distance to the neighbouring node and v_{node} is the local velocity. The safety factor f is chosen to be 5 %.

The node density changes in both space and time with the nodes being redistributed over the surface every n time steps (with $2 \leqslant n \leqslant 8$ depending on the simulation). For this, the distance between neighbouring nodes is taken inversely proportional to the local curvature and the regridding algorithm furthermore ensures that density gradients do not exceed 10 % from one segment to the next. For the jet itself we use a slightly adapted version which ensures that there is a sufficiently high resolution around the jet base and tip, but at the same time does not put an unnecessarily large number of nodes along the smooth part of the jet. To avoid numerical disturbances, we employ a regridding scheme in which at every mth time step ($2 \leqslant m \leqslant 6$) the surface nodes are completely redistributed, placing the new nodes exactly half-way between the old nodes (Oguz & Prosperetti 1993).

Three-dimensional boundary-integral methods have the advantage that contributions of surfaces far away from the region of interest decay to zero, provided that the potential there tends to a constant (which is the case in our setup). Therefore, the free surface is cut off at 100 disk radii away from the axis of symmetry and the outer walls of the container are not considered.

Small droplets which are ejected just after impact in the 'crown splash' are discarded, as described by Gekle & Gordillo (2010).

B.2. *Bubble pinch-off from an underwater nozzle*

The boundary-integral method used for these simulations is identical to the one described above. The only additional feature is the gas pressure inside the bubble which is considered uniform (i.e. inertial effects of the gas are neglected). The inflow of gas from the reservoir is modelled as described by Oguz & Prosperetti (1993) and the auxiliary material of Gekle *et al.* (2009*b*).

B.3. *Surface reconnection*

It is not possible to numerically solve in a continuous manner the transition from a single, axisymmetric cavity into two cavities. This is because radial velocities become larger and larger as the symmetry axis is approached and, consequently, it is necessary to impose an *ad hoc* cutoff radius that avoids solving length scales smaller than r_{min}. Thus, during bubble collapse we track the radial position r_i of node i which is the node closest to the axis. When $r_i < r_{min}$ a change in surface topology takes place. The single bubble surface is replaced by two separated surfaces out of which the upper and lower jets emerge. Numerically, this is achieved by shifting the neighbouring nodes $i \pm 1$ to the axis of symmetry, conserving their vertical positions as well as their potentials. Node i is discarded.

Then, cubic splines are fitted through nodes $0 \ldots i-1$ and $i+1 \ldots N$ to obtain the shape of the new surfaces. Along these splines new nodes are placed such that the jets can be resolved with a significantly higher resolution than the original bubble surfaces. We checked carefully that the involved numerical parameters do not influence the long-term jetting behaviour (except possibly r_{min} which may influence the tip of the jet, see Appendix A).

REFERENCES

Antkowiak, A., Bremond, N., Dizès, S. L. & Villermaux, E. 2007 Short-term dynamics of a density interface following an impact. *J. Fluid Mech.* **577**, 241–250.

Aristoff, J. M. & Bush, J. W. M. 2009 Water entry of small hydrophobic spheres. *J. Fluid Mech.* **619**, 45–78.

Ashley, H. & Landahl, M. 1965 *Aerodynamics of Wings and Bodies*. Addison-Wesley.

Bartolo, D., Josserand, C. & Bonn, D. 2006 Singular jets and bubbles in drop impact. *Phys. Rev. Lett.* **96**, 124501.

Bergmann, R., van der Meer, D., Gekle, S., van der Bos, A. & Lohse, D. 2009 Controlled impact of a disc on a water surface: cavity dynamics. *J. Fluid Mech.* **633**, 381–409.

Bergmann, R., van der Meer, D., Stijnman, M., Sandtke, M., Prosperetti, A. & Lohse, D. 2006 Giant bubble pinch-off. *Phys. Rev. Lett.* **96**, 154505.

Birkhoff, G. D., MacDonald, D. P., Pugh, W. M. & Taylor, G. I. 1948 Explosives with lined cavities. *J. Appl. Phys.* **19**, 563–582.

Blake, J. R. & Gibson, D. C. 1981 Growth and collapse of a vapour cavity near a free surface. *J. Fluid Mech.* **111**, 123–140.

Blake, J. R., Robinson, P. B., Shima, A. & Tomita, Y. 1993 Interaction of two cavitation bubbles with a rigid boundary. *J. Fluid Mech.* **255**, 707–721.

Bolanos-Jiménez, R., Sevilla, A., Martínez-Bazán, C. & Gordillo, J. M. 2008 Axisymmetric bubble collapse in a quiescent liquid pool. Part II. Experimental study. *Phys. Fluids* **20**, 112104.

Boulton-Stone, J. M. & Blake, J. R. 1993 Gas bubbles bursting at a free surface. *J. Fluid Mech.* **254**, 437–466.

Burton, J., Waldrep, R. & Taborek, P. 2005 Scaling instabilities in bubble pinch-off. *Phys. Rev. Lett.* **94**, 184502.

Burton, J. C. & Taborek, P. 2008 Bifurcation from bubble to droplet in inviscid pinch-off. *Phys. Rev. Lett.* **101**, 214502.

Deng, Q., Anilkumar, A. V. & Wang, T. G. 2007 The role of viscosity and surface tension in bubble entrapment during drop impact onto a deep liquid pool. *J. Fluid Mech.* **578**, 119–138.

Do-Quang, M. & Amberg, G. 2009 The splash of a solid sphere impacting on a liquid surface: numerical simulation of the influence of wetting. *Phys. Fluids* **21**, 022102.

Duchemin, L., Popinet, S., Josserand, C. & Zaleski, S. 2002 Jet formation in bubbles bursting at a free surface. *Phys. Fluids* **14**, 3000–3008.

Duclaux, V., Caillé, F., Duez, C., Ybert, C., Bocquet, L. & Clanet, C. 2007 Dynamics of transient cavities. *J. Fluid Mech.* **591**, 1–19.

Duez, C., Ybert, C., Clanet, C. & Bocquet, L. 2007 Making a splash with water repellency. *Nat. Phys.* **3**, 180–183.

Gekle, S., van der Bos, A., Bergmann, R., van der Meer, D. & Lohse, D. 2008 Non-continuous Froude number scaling for the closure depth of a cylindrical cavity. *Phys. Rev. Lett.* **100**, 084502.

Gekle, S. & Gordillo, J. M. 2010 Compressible air flow through a collapsing liquid cavity. arXiv:1001.5402v1.

Gekle, S., Gordillo, J. M., van der Meer, D. & Lohse, D. 2009*a* High-speed jet formation after solid object impact. *Phys. Rev. Lett.* **102**, 034502.

Gekle, S., Peters, I., Gordillo, J. M., van der Meer, D. & Lohse, D. 2010 Supersonic air flow due to solid–liquid impact. *Phys. Rev. Lett.* **104**, 024501.

Gekle, S., Snoeijer, J. H., Lohse, D. & van der Meer, D. 2009*b* Approach to universality in axisymmetric bubble pinch-off. *Phys. Rev.* E **80**, 036305.

Georgescu, S.-C., Achard, J.-L. & Canot, É. 2002 Jet drops ejection in bursting gas bubble processes. *Eur. J. Mech.* B **21**, 265–280.

Glasheen, J. W. & McMahon, T. A. 1996 Vertical water entry of disks at low Froude numbers. *Phys. Fluids* **8**, 2078–2083.

Gordillo, J. M. 2008 Axisymmetric bubble collapse in a quiescent liquid pool. Part I. Theory and numerical simulations. *Phys. Fluids* **20**, 112103.

Gordillo, J. M. & Gekle, S. 2010 Generation and breakup of Worthington jets after cavity collapse. Part 2. Tip breakup of stretched jets. *J. Fluid Mech.* doi:10.1017/S0022112010003538.

Gordillo, J. M., Sevilla, A. & Martínez-Bazán, C. 2007 Bubbling in a co-flow at high Reynolds numbers. *Phys. Fluids* **19**, 077102.

Gordillo, J. M., Sevilla, A., Rodríguez-Rodríguez, J. & Martínez-Bazán, C. 2005 Axisymmetric bubble pinch-off at high Reynolds numbers. *Phys. Rev. Lett.* **95**, 194501.

Grumstrup, T., Keller, J. B. & Belmonte, A. 2007 Cavity ripples observed during the impact of solid objects into liquids. *Phys. Rev. Lett.* **99**, 114502.

Gurevich, M. I. 1966 *The Theory of Jets in an Ideal Fluid*. Pergamon.

Hogrefe, J. E., Peffley, N. L., Goodridge, C. L., Shi, W. T., Hentschel, H. G. E. & Lathrop, D. P. 1998 Power-law singularities in gravity–capillary waves. *Physica* D **123**, 183–205.

Howison, S. D., Ockendon, J. R., Oliver, J. M., Purvis, R. & Smith, F. T. 2005 Droplet impact on a thin fluid layer. *J. Fluid Mech.* **542**, 1–23.

Keim, N. C., Møller, P., Zhang, W. W. & Nagel, S. R. 2006 Breakup of air bubbles in water: breakdown of cylindrical symmetry. *Phys. Rev. Lett.* **97**, 144503.

Leppinen, D. & Lister, J. R. 2003 Capillary pinch-off in inviscid fluids. *Phys. Fluids* **15**, 568–578.

Liger-Belair, G., Polidori, G. & Jeandet, P. 2008 Recent advances in the science of champagne bubbles. *Chem. Soc. Rev.* **37**, 2490–2511.

Lohse, D., Bergmann, R., Mikkelsen, R., Zeilstra, C., van der Meer, D., Versluis, M., van der Weele, K., van der Hoef, M. & Kuipers, H. 2004 Impact on soft sand: void collapse and jet formation. *Phys. Rev. Lett.* **93**, 198003.

Longuet-Higgins, M. S. 1983 Bubbles, breaking waves and hyperbolic jets at a free surface. *J. Fluid Mech.* **127**, 103–121.

Longuet-Higgins, M. S., Kerman, B. R. & Lunde, K. 1991 The release of air bubbles from an underwater nozzle. *J. Fluid Mech.* **230**, 365–390.

Longuet-Higgins, M. S. & Oguz, H. 1995 Critical microjets in collapsing cavities. *J. Fluid Mech.* **290**, 183–201.

MacIntyre, F. 1968 Bubbles: a boundary-layer 'microtome' for micron-thick samples of a liquid surface. *J. Phys. Chem.* **72**, 589–592.

Manasseh, R., Yoshida, S. & Rudman, M. 1998 Bubble formation processes and bubble acoustic signals. In *Third International Conference on Multiphase Flow, ICMF'98 Lyon, France*, pp. 1–8.

May, A. 1951 The effect of surface conditions of a sphere on its water-entry cavity. *J. Appl. Phys.* **22**, 1219–1222.

Morton, D., Rudman, M. & Liow, J. L. 2000 An investigation of the flow regimes resulting from splashing drops. *Phys. Fluids* **12**, 747–763.

Oguz, H. N. & Prosperetti, A. 1990 Bubble entrainment by the impact of drops on liquid surfaces. *J. Fluid Mech.* **219**, 143–179.

Oguz, H. N. & Prosperetti, A. 1993 Dynamics of bubble growth and detachment from a needle. *J. Fluid Mech.* **257**, 111–145.

Ohl, C. D. & Ikink, R. 2003 Shock-wave-induced jetting of micron-sized bubbles. *Phys. Rev. Lett.* **90**, 214502.

Pozrikidis, C. 1997 *Introduction to Theoretical and Computational Fluid Dynamics*. Oxford University Press.

Rein, M. 1993 Phenomena of liquid drop impact on solid and liquid surfaces. *Fluid. Dyn. Res.* **12**, 61–93.

Schmidt, L. E., Keim, N. C., Zhang, W. W. & Nagel, S. R. 2009 Memory-encoding vibrations in a disconnecting air bubble. *Nature Phys.* **5**, 343–346.

Shin, J. & McMahon, T. A. 1990 The tuning of a splash. *Phys. Fluids* A **2**, 1312–1317.

Thoroddsen, S. T. 2002 The ejecta sheet generated by the impact of a drop. *J. Fluid Mech.* **451**, 373–381.

Thoroddsen, S., Etoh, T. & Takehara, K. 2007*a* Experiments on bubble pinch-off. *Phys. Fluids* **19**, 042101.

Thoroddsen, S. T., Etoh, T. G. & Takehara, K. 2007*b* Microjetting from wave focussing on oscillating drops. *Phys. Fluids* **19**, 052101.

Thoroddsen, S., Etoh, T. & Takehara, K. 2008 High-speed imaging of drops and bubbles. *Annu. Rev. Fluid Mech.* **40**, 257–285.

Thoroddsen, S. T., Etoh, T. G., Takehara, K. & Takano, Y. 2004 Impact jetting by a solid sphere. *J. Fluid Mech.* **499**, 139–148.

Thoroddsen, S. T. & Shen, A. Q. 2001 Granular jets. *Phys. Fluids* **13**, 4–6.

Thoroddsen, S. T., Takehara, K., Etoh, T. G. & Ohl, C. D. 2009 Spray and microjets produced by focusing a laser pulse into a hemispherical drop. *Phys. Fluids* **21**, 112101.

Tjan, K. K. & Phillips, W. R. C. 2007 On impulsively generated inviscid axisymmetric surface jets, waves and drops. *J. Fluid Mech.* **576**, 377–403.

Turitsyn, K. S., Lai, L. & Zhang, W. W. 2009 Asymmetric bubble disconnection: persistent vibration evolves into smooth contact. *Phys. Rev. Lett.* **103**, 124501.

Weiss, D. A. & Yarin, A. L. 1999 Single drop impact onto liquid films: neck distortion, jetting, tiny bubble entrainment, and crown formation. *J. Fluid Mech.* **385**, 229–254.

Worthington, A. M. & Cole, R. S. 1897 Impact with a liquid surface studied by the aid of instantaneous photography. *Phil. Trans. R. Soc. Ser.* A **189**, 137–148.

Worthington, A. M. & Cole, R. S. 1900 Impact with a liquid surface studied by the aid of instantaneous photography. Paper II. *Phil. Trans. R. Soc. Ser.* A **194**, 175–199.

Yarin, A. L. 2006 Drop impact dynamics: splashing, spreading, receding, bouncing. *Annu. Rev. Fluid Mech.* **38**, 159–192.

Zeff, B. W., Kleber, B., Fineberg, J. & Lathrop, D. P. 2000 Singularity dynamics in curvature collapse and jet eruption on a fluid surface. *Nature* **403**, 401–404.